

# A Further Study of the Luminosity-Dependent Cyclotron Resonance Energies of the Binary X-ray Pulsar 4U 0115+63 with RXTE

M. Nakajima<sup>1,2</sup>, T. Mihara<sup>2</sup>, K. Makishima<sup>2,3</sup> and H. Niko<sup>3</sup>

1) *College of Science and Technology, Nihon University, 1-8-14, Kanda-Surugadai,  
Chiyoda-ku, Tokyo, JAPAN 101-0062*

2) *Cosmic Radiation, The Institute of Physical and Chemical Research, 2-1 Hirosawa,  
Wako, Saitama, JAPAN 351-0198*

3) *Department of Physics, University of Tokyo, 7-3-1 Hongo, Bunkyo-ku, Tokyo, JAPAN  
113-0033*

## ABSTRACT

The present paper reports on the *RXTE* observations of the binary X-ray pulsar 4U 0115+63, covering an outburst in 1999 March-April with 44 pointings. The 3–30 keV PCA spectra and the 15–50 keV HEXTE spectra were analyzed jointly for the cyclotron resonance features. When the 3–50 keV luminosity at an assumed distance of 7 kpc was in the range  $(5\text{--}13)\times 10^{37}$  erg s<sup>-1</sup>, harmonic double cyclotron features were observed in absorption at  $\sim 11$  and  $\sim 22$  keV, as was measured previously during typical outbursts. As the luminosity decreased below  $\sim 5\times 10^{37}$  erg s<sup>-1</sup>, the second resonance disappeared, and the fundamental resonance energy gradually increased, up to  $\sim 16$  keV at  $0.16\times 10^{37}$  erg s<sup>-1</sup>. These results reconfirm the report by Mihara et al. (2004) using *Ginga*, who observed a single absorption at  $\sim 16$  keV in a minor ( $\sim 10^{37}$  erg s<sup>-1</sup>) outburst of this object. The luminosity-dependent cyclotron resonance energy may be understood as a result of a decrease in the accretion column height, in response to a decrease in the mass accretion rate.

*Subject headings:* pulsars: binary, magnetic fields, cyclotron —X-ray: pulsars

## 1. Introduction

Accreting binary pulsars are considered to have strong surface magnetic fields in the range of several times  $10^{12}$  G. One of the methods to accurately measure their fields is to observe cyclotron resonance scattering features (CRSFs) in their X-ray spectra, because the resonance energy  $E_a$  and the magnetic field strength  $B$  are related with each other as  $E_a = 11.6 B_{12}(1 + z_g)^{-1}$  [keV], where  $B_{12}$  is the magnetic field strength in units of  $10^{12}$  Gauss and  $z_g$  is the gravitational redshift. So far, CRSFs have been detected from  $\sim 15$  X-ray pulsars, all in absorption, with balloons (e.g., Trümper et al. 1978), *HEAO-1* (Wheaton et al. 1979; White et al. 1983), *Ginga* (e.g., Clark et al. 1994; Mihara 1995; Makishima et al. 1999), *RXTE* (e.g., Coburn et al. 2002; Heindl et al. 2001), *BeppoSAX* (e.g., Santangelo et al. 1999; Orlandini et al. 1998), and other missions.

The recurrent transient 4U 0115+63, with the 3.6 s pulsations (Rose et al. 1979), is one of the X-ray pulsars whose CRSF has been studied in great detail. The optical companion is an O9e star, V635 Cassiopeae (Unger et al. 1998), with the orbital period of 24.3 days. The distance to 4U 0115+63 is estimated as 7 kpc (Negueruela and Okazaki 2001). Its CRSF was first discovered at  $\sim 23$  keV in the *HEAO-1* A4 spectra by Wheaton et al. (1979). Using the *HEAO-1* A2 data obtained in the same outburst, White et al. (1983) suggested that the 23 keV feature is in fact the second harmonic resonance, with the fundamental resonance at  $\sim 11$  keV. The suggested double harmonic structure was reconfirmed with *Ginga* by Nagase et al. (1991). Moreover, the third harmonic feature was found with *RXTE* by Heindl et al. (1999), and the fourth harmonic with *BeppoSAX* by Santangelo et al. (1999). In the *BeppoSAX* data, the resonance energies were 12.7, 24.2, 35.7 and 49.5 keV, or nearly harmonic ratios of 1:1.9:2.8:3.9. Thus, 4U 0115+63 is one of the most suitable objects to study the physics of cyclotron resonance in the polar caps of binary X-ray pulsars.

This source has been observed at various X-ray luminosity levels, and the fundamental resonance energy has been measured repeatedly at  $\sim 11$  keV. However, in a minor outburst in April 1991 observed with *Ginga*, when the 2–60 keV luminosity ( $1.9 \times 10^{37}$  erg s $^{-1}$ ) was  $\sim 7$  times lower than those typical at the outburst peaks, a drastic change in the CRSF was detected: instead of the familiar double absorption features at  $\sim 11$  keV and  $\sim 22$  keV, it exhibited a single deep and wide absorption at  $\sim 16$  keV (Mihara 1995; Mihara et al. 1998; Makishima et al. 1999; Mihara et al. 2004, hereafter Paper 1). Such a large change in  $E_a$ , presumably depending on the luminosity, had been observed neither from 4U 0115+63 itself previously, nor from other sources.

In Paper 1, we tentatively concluded that the fundamental resonance energy, at  $\sim 11$  keV in normal outbursts, increased to  $\sim 16$  keV, because a lower luminosity would make the accretion column shorter, and hence increase the magnetic field intensity at the column top.

However, there has remained an alternative possibility that the second harmonic resonance, normally at  $\sim 22$  keV, decreased to  $\sim 16$  keV in the 1991 outburst. Furthermore, even if the former interpretation is correct, the observed change in  $E_a$  was considerably larger than is predicted by an accretion column model by Burnard et al. (1991). To make the results in Paper 1 less ambiguous, we need to more densely sample the spectra as the luminosity changes over a wide range.

In this paper, we analyzed the *RXTE* data of 4U 0115+63 acquired in the 1999 March–April outburst, and studied the resonance energy as a continuous function of the luminosity in the rising and declining phases of the outburst. We have indeed detected the clear luminosity-dependent changes in the CRSF, and successfully reconfirmed the inference made in Paper 1. All of the errors appeared in this paper are 90 % confidence levels.

## 2. Observations

The outburst of 4U 0115+63 to be utilized in the present paper was detected in 1999 March with the All Sky Monitor (ASM) on board *RXTE*. Figure 1 shows the light curve of the whole outburst. The peak intensity,  $\sim 30$  c s $^{-1}$ , corresponds to approximately 400 mCrab, which is typical of regular outbursts of this source. The *BeppoSAX* observation of this outburst led to the discovery of the four harmonic CRSFs by Santangelo et al. (1999).

During this outburst, 44 short ( $\sim 1$  ksec) pointing observations were made with the Proportional Counter Array (PCA; Jahoda et al. 1996) and the High-Energy X-ray Timing Experiment (HEXTE; Rothschild et al. 1998) on board *RXTE*, starting on 1999 March 3 and ending on April 20. Heindl et al. (1999) utilized these datasets, and successfully detected up to three CRSFs. The PCA consists of five xenon proportional counter units (PCUs) with an energy range of 2–60 keV and a total effective area of  $\sim 7000$  cm $^2$ . In order to extend the detector life time, some of the PCUs were not operated in the present observations. In this paper, we utilize all PCUs operated at each observation, as summarized in Table 1. The HEXTE consists of two arrays (cluster A and B) of four NaI/CsI scintillation counters, with an energy range of 15–250 keV and a total effective area of  $\sim 1600$  cm $^2$ . However, one pulse height analyzer of cluster B failed in the early mission phase, so its effective area is approximately 3/4 of the nominal value.

From the 44 pointing observations of the 1999 outburst in the *RXTE* archive, we selected 34 data with low electron contamination; these are listed in Table 1. In this selection, we set the electron-rate threshold at 0.12 counts s $^{-1}$  (which is a typical value when the signal X-ray flux is high), in order not to discard good data by mistaking signal X-rays for electrons. In

order to complement the rather high threshold, we visually inspected the electron-rate light curves, and confirmed that none of the 34 datasets are contaminated by sporadic electron events. We then selected the Standard-2 mode data which have 16 s time resolution and 129 energy channels, and used only the top layer of the PCA which has a low background. We employed FTOOLS v5.2 for analysis, and used the calibration data file epoch 3 and 4 to make the energy response matrix. The background subtraction utilized so-called bright background model for all data. We have selected those data acquired when the offset angle of the source to the field of view center was  $< 0^\circ.02$ , the earth elevation angle was  $> 10^\circ$ , and the spacecraft was not within 30 minutes of an entrance from the South Atlantic Anomaly. The net exposure of each datasets, which was obtained after these screenings, is also given in Table 1.

Since different observations used different sets of PCUs (Table 1), it is important to evaluate systematic errors associated with the PCA responses (particularly among different PCUs). Accordingly, we followed Wilms et al. (1999) and Coburn et al. (2001), and analyzed the Crab nebula data obtained on 1997 December 12 (for epoch 3) for  $2.8 \sim 5.4$  ksec, and 1999 December 18 (for epoch 4) for  $1.9 \sim 8$  ksec, with the exposure depending on PCUs. By fitting these data with a single power-law of photon index 2.1, which is known to be a good approximation of the Crab spectrum in the PCA range, we examined how the data-to-model ratio at each energy bin scatters among the PCUs. From this, we have set the systematic error of the PCU to be 1 %. The subsequent results do not change if we instead use 0.5 %.

### 3. Analysis and Results

#### 3.1. Ratios to the Crab spectrum

For each dataset listed in Table 1, we accumulated 3–30 keV PCU data into a single spectrum, and 15–50 keV HEXTE data into another. The background was subtracted in the way described in section 2. In order to grasp the spectral shape in a model-independent manner without being hampered by the instrumental response, we surveyed these spectra normalized to that of the Crab spectrum. The reference Crab data are the same as utilized to estimate the systematic error. The results are shown in Figure 2, where errors which propagated from the Crab spectrum are negligible.

In Figure 2, the first data set acquired on March 3 gives a relatively featureless spectral ratio. When the flux increased and exceeded  $710 \text{ c s}^{-1} (\text{PCU})^{-1}$  on March 5, the Crab ratio started to reveal two dip features at  $\sim 12$  keV and  $\sim 25$  keV. These can be interpreted as the fundamental and second harmonic, as have been observed repeatedly. The double absorption

feature persisted throughout the flare peak until March 29. However, when the flux decreased to  $\leq 400 \text{ c s}^{-1} (\text{PCU})^{-1}$  on April 2, it turned into an apparently single absorption feature. Thus, the present data appears to reconfirm the *Ginga* results reported in Paper 1, that the CRSF appears in double absorption when the X-ray intensity is high, while it changes into a single absorption as the source becomes faint. In the *RXTE* data, the threshold is suggested to lie between 400 and 710  $\text{c s}^{-1} (\text{PCU})^{-1}$ . Below, we attempt to quantitatively confirm these inspections.

### 3.2. Analysis of representative spectra

It is known that typical continuum spectra of accreting binary pulsars can be approximated with a power-law times exponential cutoff model. In this paper, we employ its updated version called NPEX (Negative and Positive power-laws with EXponential) model (Mihara 1995; Makishima et al. 1999), and fit the background-subtracted spectra in comparison with the results reported in Paper 1. The NPEX model is written as

$$NPEX(E) = (A_1 E^{-\alpha_1} + A_2 E^{+\alpha_2}) \exp\left(-\frac{E}{kT}\right), \quad (1)$$

where  $E$  is the X-ray energy in units of keV,  $A_1$  and  $\alpha_1$  are the normalization and photon index of the negative power-law, respectively,  $A_2$  and  $\alpha_2$  are those of the positive power-law, and  $kT$  represents the cutoff-energy in units of keV. In this paper, we tentatively fix  $\alpha_2$  at 2.0, so that the positive power-law describes a Wien peak (Rybicki & Lightman 1979).

Figure 3 shows the pulse-phase-averaged PCA+HEXTE spectra obtained on March 27 and April 8, when the Crab ratio suggests the double and single CRSF, respectively (see Figure 2). We first attempted to fit the spectra with the NPEX model. In order to take into account possible over- or under-subtraction of background, we allowed the background normalization to vary (as described in the *RXTE cook book*), so as to minimize the fit chi-squared. We found the optimum normalization factor to be close to the nominal value of 1.0 within a few percent. Even allowing this correction, the model left significant structures in data-to-model ratios as shown in Figure 3d and g. As a result, the fits remained unacceptable with  $\chi_\nu^2 \sim 62$  and  $\chi_\nu^2 \sim 30$  for the March 27 and April 8 spectra, respectively. Indeed, the March 27 spectrum exhibits two negative deviations at  $\sim 12$  and  $\sim 22$  keV from the NPEX fit, while that of April 8 shows only one negative feature around 16 keV. These results reconfirm the inference from the Crab ratios.

In order to better reproduce the spectra, we next introduced a cyclotron absorption

(CYAB) factor which is given as

$$CYAB(E) = \exp \left\{ -\frac{\tau (WE/E_a)^2}{(E - E_a)^2 + W^2} \right\}, \quad (2)$$

where  $E_a$  is the resonance energy,  $W$  is the width of the absorption structure, and  $\tau$  is the depth of the resonance (Mihara et al. 1990). We fitted the spectrum on March 27 with the NPEX continuum multiplied by two CYAB factors (hereafter NPEX×CYAB2 model), in which all the NPEX and CYAB parameters are left free except that the second CRSF energy is fixed at twice the fundamental energy. For the spectrum on April 8, we applied the NPEX multiplied by a single CYAB factor (hereafter NPEX×CYAB model). The PCA+HEXTE data were fitted simultaneously with the same parameters, but using another free parameter to adjust relative normalizations of the two instruments. The background normalization was again allowed to vary, by up to  $\pm 1.5$  %. We did not include low energy absorption nor Fe-K line, since our spectra exhibit neither low-energy turn-offs nor an excess around 6.4 keV. The lack of significant Fe-K line is often noticed among transient X-ray pulsars with Be-type primary stars (e.g., Nagase 1989); in such a system, the matter to be accreted by the pulsar presumably forms a disk-shaped envelope around the Be star, and hence its solid angle as seen from the pulsar is much smaller than the case where the matter is captured from a more isotropic stellar wind.

As shown in Figure 3e and f, the NPEX×CYAB model has successfully reproduced the PCA+HEXTE data on April 8, yielding reduced chi-squared of  $\sim 1.2$ . The background correction factor turned out to be 0.3 %. In contrast, the March 27 spectrum was not reproduced successfully ( $\chi_\nu^2 \sim 2.0$ ) even by the NPEX×CYAB2 model, because of negative residuals around 35 keV (Figure 3c). This feature was removed by multiplying a third CYAB factor, of which the centroid energy is  $32.8_{-8.3}^{+3.2}$  keV. Since this energy is close to  $3 \times E_{a1}$ , the feature can be identified with the third harmonic resonance detected from the same outburst (Heindl et al. 1999; Santangelo et al. 1999). We hence fitted the March 27 spectrum with the NPEX continuum multiplied by three CYAB factors, of which the resonance energies were constrained to have harmonic ratios (1 : 2 : 3). This model, hereafter called NPEX×CYAB3 model, successfully reproduced the March 27 spectrum with  $\chi_\nu^2 \sim 1.2$ . The derived fundamental resonance energy on March 27 is  $10.4 \pm 0.1$  keV at an X-ray luminosity of  $7.6 \times 10^{37}$  erg s $^{-1}$ , while that of April 8 is  $14.2 \pm 0.4$  keV at  $3.0 \times 10^{37}$  erg s $^{-1}$ . The resonance energy has thus increased by a factor of 1.4 as the luminosity decreased by a factor of 2.5, although there still remains a possibility that the single CRSF at 14.2 keV on April 8 is in reality the second harmonic.

While we tentatively fixed  $\alpha_2$  at 2.0, Santangelo et al. (1999) obtained  $\alpha_2 = 0.41 \pm 0.05$  by analyzing the *BeppoSAX* data of the same outburst. This is probably due to difference

in the energy band used; we fitted the spectra in the 3 – 50 keV range, while Santangelo et al. (1999) in 9 – 100 keV. To examine this difference, and to examine whether the constraint of  $\alpha_2 = 2.0$  is justifiable, we fitted the NPEX  $\times$  CYAB3 model, with  $\alpha_2$  left free, to the PCA+HEXTE data on March 19a, which is one of those with the highest statistics. Then, this parameter has been constrained as  $\alpha_2 = 1.60 \pm 0.99$ , which includes the fiducial value of 2.0. More specifically, fixing  $\alpha_2$  at 2.0, at our best fit value of 1.60, and at the *BeppoSAX* value of 0.41, gave a reduced chi-squared of 1.29 ( $\nu = 78$ ), 1.33 ( $\nu = 77$ ), and 1.67 ( $\nu = 78$ ), respectively. Based on these results, we hereafter retain our initial assumption of  $\alpha_2 = 2.0$ .

Apart from the continuum modeling, we must examine whether the CRSF parameters we have derived are consistent with the previous analyses of the same outburst (Heindl et al. 1999; Santangelo et al. 1999). We therefore analyzed the PCA+HEXTE spectra on March 11.36–11.40 (Obs. 7; Table 1), in comparison with those reported by Heindl et al. (1999) for a particular pulse phase (0.70–0.76 in terms of their phase convention) on March 11.87–12.32. We found some difference in the resonance energy;  $10.6_{-0.2}^{+0.1}$  keV from our fit, while  $12.40_{-0.35}^{+0.65}$  keV by Heindl et al. (1999). The difference is likely to arise from the different modeling of the CRSF employed in these studies, because Heindl et al. (1999) used a Gaussian absorption model whereas we are using the CYAB factor. Accordingly, we re-fitted the same spectra with an NPEX model multiplied by two Gaussian absorption models. The fundamental cyclotron resonance was then obtained at  $E_{a1} = 12.3 \pm 0.1$  keV, which is consistent with Heindl et al. (1999). The higher accuracy of our result is probably because we analyzed the pulse phase-averaged spectra. Other resonance parameters turned out to be consistent between the two works. We thus conclude that our results are consistent with those of Heindl et al. (1999) using the longer exposure, and have comparable accuracy.

### 3.3. Analysis of date-sorted spectra

For the moment, we mainly concentrate on the study of the 3–30 keV PCA spectra, because this energy range is most relevant to the CRSFs. In order to more continuously resolve the drastic spectral change between March 27 to April 8, we applied the NPEX model (without incorporating CYAB factors) to the daily-averaged PCU0+PCU2+PCU3 spectra over this period. Figure 4a shows ratios of the data to the best-fit NPEX model, which allow us to grasp the spectral changes objectively. The PCA background normalizations were corrected in the way as described in section 3.2. Since the ratio on March 27 and 29 shows almost the same shape as Figure 3d, we may consider that the two CRSF persisted at least until March 29. On March 31, the second CRSF became less clear, and on April 2 onward, the ratio reveals only a single absorption. In addition, the fundamental resonance

initially observed at  $\sim 11$  keV moved to higher energies, up to  $\sim 15$  keV, while there is no opposite trend such as the two features drifting toward lower energies.

In order to quantify the results of these visual inspections, we have fitted the same set of spectra with the NPEX×CYAB2 (or NPEX×CYAB) model. The obtained best-fit parameters are summarized in Table 2, and the ratio of the data to the model are plotted in Figure 4b. The spectra from March 27 through April 2 all required the two CYAB factors, because the double CYAB fit gave a significantly better reduced chi-square ( $0.6\sim 1.2$ ) than the single CYAB case ( $\geq 2$ ). On April 4, the spectrum is roughly reproduced by the single CYAB model, although there remains a hump at  $\sim 23$  keV which does not disappear by including the second CYAB factor. The successful single CYAB fit continued to the end, on April 8. These results quantitatively confirm our inference made above, that the fundamental CRSF energy increased from 10 to 15 keV over this  $\sim 10$  day period as assumed in Paper 1, although details of the change are not yet resolved clearly.

### 3.4. Analysis of intensity-sorted spectra

Although the 3–30 keV spectrum apparently depends on the luminosity, the source exhibits significant intra-day variations, as shown in Figure 5. As a result, each spectrum in Figure 4, in reality, is an average over a relatively wide luminosity range. In order to see the luminosity dependence more clearly, we sorted the PCA data from March 27 to April 8 into 8 intensity intervals, in reference to Figure 5. We again used data from PCU 0, 2 and 3, which worked throughout this period. Then, we have repeated the same analysis as performed in section 3.3.

Figure 6a shows the ratios of these intensity-sorted spectra to their best-fit NPEX models, to be compared with Figure 4a. The two CRSFs, at  $\sim 11$  keV and  $\sim 22$  keV, are thus observed clearly in the higher four intensity levels, f1 through f4. As the intensity decreased, the second CRSF gradually became shallower. Finally, the second CRSF disappeared at level f6, and the fundamental CRSF started to move from  $\sim 11$  to  $\sim 16$  keV over levels f5 through f8. From these results, we confirm that the  $\sim 16$  keV single structure results from an upward shift of the  $\sim 10$  keV fundamental CRSF. The spectral changes revealed here are consistent with, but clearer than, those seen between April 2 and April 4 in the date-sorted spectra.

Using the NPEX×CYAB2 (or NPEX×CYAB) model, we quantified the CRSF parameters as a function of the intensity. The fitting results are summarized in Table 3, and the ratios of the data to the model are shown in Figure 6b. The full fitting results are displayed

in Figure 7. The two CYAB factors have been required by the f1 to f4 spectra. The second CRSF is not clearly visible in the f5 ratio (Figure 6a and Figure 7), but a large  $\chi_\nu^2$  ( $\sim 2.0$ ) was obtained by the single CYAB fitting. We therefore applied the NPEX×CYAB2 model to the f5 spectrum, and obtained a fully acceptable fit (Table 3). This means that the second harmonic is still present in the f5 spectrum, with a reduced depth ( $\tau_2 \simeq 0.2$ ). From f1 through f5, both  $\tau_2$  and  $W_2$  decreased; that is, the second harmonic feature became narrower and shallower. Although this behavior is absent in the day-sorted results (Table 2), the difference can be attributed to the fact that each day-average spectrum is a mixture of different spectra corresponding to different intensities. The f6 through f8 spectra have been fitted successfully by the NPEX×CYAB model.

These results unambiguously show that the center energy of the fundamental CRSF moved from 10 to 15 keV as the luminosity decreased. Thus, we can conclude that the 16 keV spectral structure of 4U 0115+63 observed by *Ginga* (1991) and this work is the fundamental CRSF, rather than the second harmonic resonance which moved toward lower energies. The threshold between the single and double CRSF structures is found at a 3 – 30 keV luminosity of  $\sim 4.2 \times 10^{37}$  erg s<sup>-1</sup>.

### 3.5. Analysis of all PCA and HEXTE spectra

Now that we have understood the basic behavior of the CRSFs, we now proceed to the analysis of the entire PCA and HEXTE data prepared in section 3.1. Since the Crab ratios on March 3 and 4 do not show clear CRSFs (Figure 2), we first attempted an NPEX fitting, but the model was unacceptable ( $\chi_\nu^2 \geq 20$ ), because of the negative deviation at  $\sim 15$  keV. Then we applied the NPEX×CYAB model to these data, but the fit was still unacceptable ( $\chi_\nu^2 \geq 1.7$ ). Finally, we fitted these data with the NPEX×CYAB2 model, and obtained reasonable fit with  $\chi_\nu^2 \leq 1.3$ . These results imply that the double CRSFs were already present in these early data sets, with the fundamental resonance at  $\sim 12$  keV as given in Table 4. Thus, the data from the beginning through April 2 were generally well described with the NPEX×CYAB2 model. By jointly analyzing the PCA and HEXTE data, the second CRSF parameters have been significantly better constrained than using the PCA data alone. The derived parameters are listed in Table 4.

In some fits, however, we were still left with rather large values of  $\chi_\nu^2$ . For example, the NPEX×CYAB2 fits are rather poor ( $\chi_\nu^2 \geq 1.5$ ) on March 15, 19a, 21a, 22, 27, 29 and 31 (Table 4), often with negative residuals at  $\sim 35$  keV. Like in Figure 3b, these residuals can be mostly removed by multiplying the model with a third CYAB factor. Typical parameters of the third CRSF, e.g., observed on March 19a, are  $E_{a3} = 35.2 \pm 2.2$  keV,  $W_3 = 9.3 \pm 2.5$

keV and  $\tau_3 = 0.6 \pm 0.1$ . We can hence identify it with the third harmonic, after section 3.2. The third harmonic persisted in the spectra for about half a month from March 15, with relatively constant parameters, till March 31 when it became unconstrained presumably due to insufficient data statistics in higher energies. Meantime, the second CRSF stayed at around 22 keV.

The data from April 3 to the end did not show the higher harmonics, with the NPEX×CYAB model giving acceptable fits ( $\leq 1.4$ ). In order to estimate the upper limits on the second harmonic feature, we attempted to fit the data obtained from April 3 to April 8 with the NPEX×CYAB2 model. In addition to the constraint of  $E_{a2} = 2E_{a1}$  employed so far, the second CRSF width  $W_2$  was tied to  $W_1$ , because  $W_2$  is close to  $W_1$  (except for April 1 and 2) when the spectrum exhibits the double features. The obtained upper limits on  $\tau_2$  are given in Table 4.

From these studies using the PCA and HEXTE data, we reconfirmed that the cyclotron resonance energies increase as the X-ray luminosity decreases. These results are consistent with those derived in section 3.4 from the intensity-sorted study of the 3 – 30 keV PCA spectra. Figure 8 summarizes the fundamental resonance energies, derived through both the date-sorted and intensity-sorted analyses, as a function of the calculated 3 – 50 keV luminosity at 7 kpc.

## 4. Discussion

We have analyzed the 34 PCA+HEXTE datasets, covering the whole 1999 March-April outburst of 4U 0115+63 in which the 3 – 50 keV source luminosity changed over  $L_x = (0.17 - 14) \times 10^{37}$  erg s<sup>-1</sup>. When  $L_x > 7 \times 10^{37}$  erg s<sup>-1</sup>, we observed the familiar double CRSFs with  $E_{a1} \simeq 11$  keV. As  $L_x$  decreased across a rather narrow range of  $(5 \pm 2) \times 10^{37}$  erg s<sup>-1</sup>, the second harmonic resonance disappeared, and the fundamental resonance energy increased from  $E_{a1} \sim 11$  keV to  $\sim 16$  keV. These results reconfirm Paper 1, and unambiguously reveal that the resonance energy *increases* as the source gets less luminous.

### 4.1. The resonance energy variations

Except for some hysteresis effects between the rising and decay phases of the outburst,  $E_{a1}$  changes roughly as a single-valued function of  $L_x$ . In particular, the intensity-sorted 3–30 keV PCA spectra and the date-sorted PCA+HEXTE data imply consistent results. Furthermore, the *Ginga* results reported in Paper 1 fall on the same  $E_{a1}$  vs.  $L_x$  relation.

Therefore, the phenomenon is inferred to have a good reproducibility as a function of the luminosity.

The CRSF is known to depend also on the pulse phase, presumably because different scattering regions characterized by slightly different magnetic field strengths are observed as the neutron star rotates. When studying luminosity-related changes in the resonance energy, such pulse-phase dependent effects must be considered. In the case of 4U 0115+63, however, the phase dependent variation of  $E_{a1}$  in the 1999 outburst was relative small,  $\sim 10\%$  (Santangelo et al. 1999). Furthermore, the phase-resolved analysis performed in Paper 1, on the two different luminosity levels, did not affect the main results from the phase-averaged spectroscopy. We therefore concentrate, in the present paper, on the phase-averaged analysis.

As mentioned in Paper 1, luminosity-dependent changes of the accretion column height provide the most likely explanation to our results, because the column is expected to become taller as the source luminosity increases (e.g., Burnard et al. 1991). Assuming that the CRSF is formed at a height  $h_r$  above the neutron star surface in the accretion column, and the magnetic field strength there follows the dipole law, we then expect

$$E_{a1} \propto (R_{\text{NS}} + h_r)^{-3}(1 + z_g)^{-1} \quad (3)$$

with  $R_{\text{NS}}$  the radius of the neutron star. The factor  $(1 + z_g)$  describes the gravitational redshift, but below we assume  $z_g = 0$  for simplicity. Then, the relative resonance height,  $h_r/R_{\text{NS}}$ , can be related to the resonance energy as

$$\frac{h_r}{R_{\text{NS}}} \approx \left( \frac{E_a}{E_0} \right)^{-1/3} - 1, \quad (4)$$

where  $E_0$  is the resonance energy to be observed on the neutron star surface.

Substituting the observed value of  $E_{a1}$  into Equation (4), we have calculated  $h_r/R_{\text{NS}}$  as a function of the X-ray luminosity. The results are shown in Figure 9. Since there is no *a priori* knowing of  $E_0$ , we employed two different values of  $E_0$ ; 18 keV and 20 keV, the former close to the observed maximum value of  $E_{a1}$ . Except for some differences between the two assumptions on  $E_0$ , the height  $h_r$  thus increases in a rough proportion to the X-ray luminosity, up to  $\sim 7 \times 10^{37}$  erg  $s^{-1}$  where  $h_r$  appears to saturate at  $\sim 0.2R_{\text{NS}}$ . In addition,  $h_r/R_{\text{NS}}$  may approach a finite value of  $0.03 \sim 0.07$ , instead of zero, as  $L_x$  decreases below  $\sim 2 \times 10^{37}$  erg  $s^{-1}$ .

The results presented in Figure 9 may be compared to a theoretical prediction by Burnard et al. (1991), who calculated the height of the accretion column  $h_{\text{top}}$  as

$$\frac{h_{\text{top}}}{R_{\text{NS}}} \approx \frac{L_x}{L_{\text{Edd}}^{\text{eff}} H_{\perp}}. \quad (5)$$

Here,  $L_{\text{Edd}}^{\text{eff}}$  is the Eddington luminosity along the magnetic field which is identical to the conventional Eddington Luminosity for a  $1.4M_{\odot}$  neutron star,  $L_{\text{Edd}}^{\text{eff}} = 2.0 \times 10^{38}$  ergs  $\text{s}^{-1}$ , and  $H_{\perp}$  is the ratio of the Thomson cross section to the Rosseland-averaged electron scattering cross section for radiation flows across the magnetic fields. The dashed line in Figure 9 shows this prediction, assuming  $H_{\perp} = 1.23$  (Paper 1) and  $R_{\text{NS}} = 10$  km. Except for the observed saturation toward the highest luminosity and  $\lesssim 2 \times 10^{37}$  erg  $\text{s}^{-1}$ , the value of  $h_{\text{r}}$  measured at each luminosity level thus corresponds to  $\sim 70\%$  of the predicted  $h_{\text{top}}$ . This is quite reasonable, because the resonance energy is expected to sample the magnetic field strength which is measured at, or slightly below, the top of the column (i.e.,  $h_{\text{r}} \lesssim h_{\text{top}}$ ).

So far, we have assumed that the observed X-ray intensity changes are caused solely by actual variations of the intrinsic source luminosity. However, the intensity may also be affected by other extrinsic factors, such as partial obscuration by materials around the accretion disk. Such effects are known, e.g., in Her X-1 (Mihara et al. 1991). In the present outburst of 4U 0115+63, Heindl et al. (1999) detected occasional appearance of “mHz QPO”, with a period of  $\sim 500$  sec and intensity changes up to  $\sim 40\%$ , and suggested that the phenomenon is possibly due to source obscuration by some ionized materials. If so, we would need a caution in interpreting the results from our intensity-sorted analysis.

In order to investigate effects of the mHz QPO on our results, we inspected PCA light curves acquired over the period used for our intensity-sorted analysis (March 27 through April 8). As shown in the inset to Figure 10, a relatively clear QPO was found on March 31, although the period is about 1000 sec instead of the 500 sec reported by Heindl et al. (1999). Then, we sliced the light curves as shown there, and produced a pair of PCA spectra corresponding to peaks and valleys of the QPO. Figure 10 presents these spectra and their ratio, as well as residuals when fitted individually with the NPEX model. The resonance energy thus clearly increases at the QPO valley. By fitting the spectra with the NPEX times CYAB2 model (with  $W_2$  again fixed at  $W_1$ ), we have constrained the resonance centroid as  $10.4_{-0.7}^{+0.2}$  keV at the QPO peak with  $L_{\text{x}} = 8.2 \times 10^{37}$  erg  $\text{s}^{-1}$ , and  $11.8_{-0.5}^{+0.9}$  keV at the QPO bottom with  $L_{\text{x}} = 5.2 \times 10^{37}$  erg  $\text{s}^{-1}$ . Thus, the energy shift is statistically significant. Furthermore, these two data points line up in Figure 8 closely on the general  $L_{\text{x}}$  vs.  $E_{\text{a1}}$  correlation from the day-sorted and intensity-sorted analysis. We hence conclude that our basic results remain unaffected, and that the QPO, at least on this occasion, is likely to reflect real changes in the intrinsic luminosity rather than some obscuration effects. This inference is reinforced by the relatively flat spectral ratio, because the ratio should show an increased low-energy absorption if the obscuration were due to neutral material, or Fe-K edge feature if it were highly ionized.

## 4.2. Behavior of the other parameters

So far, many authors (e.g. Paper 1 and Coburn et al. 2002) studied relations among the continuum and cyclotron line parameters. Our work provides a valuable opportunity to investigate how these parameters in a single system change in correlated ways, when the resonance energy varies. Among various correlations, a particularly interesting one is that between  $\tau$  and the  $W/E_a$  ratio; in fact, Coburn et al. (2002) found a positive correlation between them over a large sample of phase-averaged spectra of X-ray pulsars. Later, Kreykenbohm et al. (2004) noticed that the same correlation holds for the phase-resolved spectra of GX 301-2, and argued that the correlation may be explained if the accretion column has a tall cylindrical shape rather than flat coin-shaped geometry. As presented in Figure 11, the fundamental and second harmonic widths of 4U 0115+63 from the present observations both depend positively on their respective resonance depths, in agreement with the correlation found by Coburn et al. (2002). These results, together with the argument by Kreykenbohm et al. (2004), strengthen the tall cylindrical column geometry which we invoked in § 4.1. For reference, we did not find particular correlations between  $E_a$  and  $kT$ , or between  $E_a$  and  $W$ .

Figure 12 shows the spectral parameters as a function of the X-ray luminosity. There, the positive  $\tau$  vs.  $W/E_a$  correlation of Figure 11 has been decomposed into luminosity dependent changes in  $W/E_a$  (panel a) and  $\tau$  (panels c, d). Up to  $\sim 4 \times 10^{37}$  erg s<sup>-1</sup>,  $\tau_1$  thus stays relatively constant, with a hint of mild increase presumably due to the increased column density in the emission region. Over the same luminosity range, the fractional width  $W_1/E_{a1}$  increases more clearly. This would not be due to changes in the Doppler broadening (e.g. Mészáros 1992), since the NPEX  $kT$  parameter shown in Figure 12b, which is thought to approximate the electron temperature in the emission region (Mihara et al. 2004; Makishima et al. 1999), stays rather constant. Instead, the increase in the  $W_1/E_{a1}$  ratio could be a result of the luminosity-correlated elongation in the accretion column, which would cause a larger range of magnetic field intensities to participate in the resonance formation.

Beyond  $\sim 4 \times 10^{37}$  erg s<sup>-1</sup>, both  $\tau_1$  and  $W_1/E_{a1}$  start decreasing clearly, while the 2nd harmonic resonance develops rapidly both in depth ( $\tau_2$ , Figure 12d) and relative width ( $W_2/E_{a2}$  in Figure 12a). In short, the CRSF makes a transition from the single feature at low luminosities to the harmonic double feature at higher luminosities. Since this occurs approximately over the luminosity range where the rapid change in  $E_{a1}$  takes place, we consider that the single-to-double transition of the CRSF has the same origin as the resonance energy shift.

The behavior of the fundamental and 2nd harmonic parameters at the single-to-double transition may reflect basic differences in their elementary processes. The fundamental

resonance has a very large cross section, but it acts as scattering rather than absorption, because an electron which is excited by absorbing a photon of energy  $\sim E_{a1}$  will immediately return to the ground state by emitting a photon of nearly the same energy. The second harmonic resonance, though with a much smaller cross section, will in contrast act as pure absorption, because the electron excitation/deexcitation in this case occurs via absorption of a photon of energy  $\sim 2E_{a1}$  and cascade emission of two photons of energies  $\sim E_{a1}$  each. The emitted photons will fill up the fundamental resonance, making it shallower (so-called two-photon effects; Alexander & Meszaros 1991). In the present case, the accretion column may be effectively thick to the fundamental resonance ( $\tau_1 > 1$ ) essentially at all the observed luminosities, but presumably optically thin ( $\tau_2 \ll 1$ ) to the second resonance photons when the luminosity is low and hence the accretion column is short. As the source luminosity increases, the column becomes taller and opaque to the second resonance, leading to the emergence of the second resonance feature. At the same time, the two-photon effect would reduce  $\tau_1$ , just as seen in Figure 12c. A similar effect was observed in the *INTEGRAL* spectrum of GX 301 – 2 by Okada et al. (2004), who reported that  $\tau_1$  of its  $\sim 35$  keV CRSF decreased toward higher luminosities.

### 4.3. The case of X0331+53

Although 4U 0115+63 thus provides the first clear example of luminosity-dependent changes of the cyclotron resonance energy, there has emerged another promising case. This is the transient X-ray pulsar X0331+53 (V0332+53), from which a very prominent CRSF was detected with *Ginga* at  $E_a = 28.5 \pm 0.5$  keV together with a hint of the second harmonic (Makishima et al. 1990). This was observed in an outburst when the 2 – 60 keV luminosity was  $\sim 2 \times 10^{37}$  erg s<sup>-1</sup> at an assumed distance of 3 kpc. A re-analysis of the same data using the NPEX continuum have revised the value slightly to  $E_a = 27.2 \pm 0.3$  keV (Makishima et al. 1999).

The object entered a bright outburst from 2004 November, becoming considerably more luminous than was observed with *Ginga* (Swank et al. 2004; Remillard 2004). Observations with *INTEGRAL* (Kreykenbohm et al. 2005) and *RXTE* (Coburn et al. 2004) have clearly reconfirmed the fundamental CRSF, and further revealed the second and third resonances. The fundamental resonance energy obtained with *INTEGRAL* is  $24.9 \pm 0.1$  keV (Kreykenbohm et al. 2005) at a 3 – 50 keV luminosity of  $\sim 8 \times 10^{37}$  erg s<sup>-1</sup>. This means that a factor 4 increase in the luminosity (from the *Ginga* outburst to the present one) is accompanied by a  $\sim 10\%$  decrease in  $E_{a1}$ . As mentioned by Mihara et al. (2004), the same effect was already visible between two pointings with *Ginga*. For comparison, the resonance energy

of 4U 0115+63 changes by a somewhat larger amount ( $\sim 20\%$ ) across the same factor 4 luminosity range (Figure 8). The archival *RXTE* data of X0331+53 are currently being analyzed, and the results will be reported elsewhere (Nakajima et al. , in preparation).

Now, we have two examples of luminosity dependent changes in the resonance energy. However, there is an apparent counter example, namely Her X-1. In a large amount of *RXTE* data covering its “main on” phase, the 2 – 30 keV luminosity (at 5.8 kpc) of Her X-1 varied by a factor of 2 over  $(1.8 - 3.2) \times 10^{37}$  erg  $s^{-1}$ , but the CRSF stayed at  $\sim 40$  keV (Gruber et al. 2001). One possible interpretation of these results on Her X-1 is that its luminosity swing was not large enough to reach the critical range (*cf.* Figure 8) where  $E_a$  starts changing significantly. Alternatively, the luminosity-related changes in the CRSF may depend on the object, for some reasons which are yet to be detailed.

In conclusion, our study using the *RXTE* data has confirmed the inference made in Paper 1, that the cyclotron resonance energy of 4U 0115+63 increases as the X-ray luminosity decreases. While this provide a new tool with which we can diagnose the accretion column of strongly magnetized neutron stars, it remains yet to be confirmed whether the phenomenon is common among this type of objects.

## REFERENCES

- Alexander, S. G., & Meszaros, P. 1991, *ApJ*, 372, 565
- Bildsten, L., Chakrabarty, D., Chiu, J., Finger, M. H., Koh, D. T., Nelson, R. W., Prince, T. A., Rubin, B. C., Scott, D. M., Stollberg, M., Vaughan, B. A., Wilson, C. A., & Wilson, R. B., 1997, *ApJ*, 113, 367
- Burnard, D. J., Arons, J., & Klein, R. I. 1991, *ApJ*, 367, 575
- Clark, G. W., Woo, J. W., & Nagase, F. 1994, *ApJ*, 422, 336
- Coburn, W., Heindl, W. A., Gruber, D. E., Rothschild, R. E., Staubert, R., Wilms, J., & Kreykenbohm, I. 2001, *ApJ*, 552, 738
- Coburn, W., Heindl, W. A., Rothschild, R. E., Gruber, D. E., Kreykenbohm, I., Wilms, J., Kretschmar, P., & Staubert, R. 2002, *ApJ*, 580, 394
- Coburn, W., Kalemci, E., Kretschmar, P., Kreykenbohm, I., Rothschild, R., Staubert, R., & Wilms, J. 2004, *Atel*, 381, 1
- Finger, M. H., Wilson, R. B., & Harmon, B. A. 1996, *ApJ*, 459, 288

- Heindl, W. A., Coburn, W., Gruber, D. E., Pelling, M. R., Rothschild, R. E., Wilms, J., Pottschmidt, K., Staubert, R. 1999 , ApJ, 521, L49
- Heindl, W. A., Coburn, W., Gruber, D. E., Rothschild, R. E., Kreykenbohm, I., Wilms, J., & Staubert, R. 2001 , ApJ, 563, L35
- Jahoda, K., Swank, J. H., Giles, A. B., Stark, M. J., Strohmayer, T., Zhang, W., & Morgan, E. H. 1996, Proc. SPIE, 2808, 59
- Kreykenbohm, I., Coburn, W., Wilms, J., Kretschmar, P., Staubert, R., Heindl, W. A., & Rothschild, E. 2002, A&A, 395, 129
- Kreykenbohm, I., Mowlavi, N., Produit, N., Soldi, S., Walter, R., Dubath, P., Lubinski, P., Trümper, M., Coburn, W., Santangelo, A., Rothschild, R. E., & Staubert, R. 2005, A&A, 433, L45
- Makishima, K., Mihara, T., Ishida, M., Ohashi, T., Sakao, T., Tashiro, M., Tsuru, T., Kii, T., Makino, F., Murakami, T., Nagase, F., Tanaka, Y., Kunieda, H., Tawara, Y., Kitamoto, S., Miyamoto, S., Yoshida, A., & Turner, M. J. L. 1990, ApJ, 365, L59
- Makishima, K., Mihara, T., Nagase, F. & Tanaka, Y. 1999, ApJ, 525, 978
- Mészáros, P. 1992, High-Energy Radiation from Magnetized Neutron Stars (Chicago: Univ. Chicago Press)
- Mihara, T., Makishima, K., Ohashi, T., Sakao, T., & Tashiro, M. 1990, *Nature*, 346, 250
- Mihara, T., Ohashi, T., Makishima, K., Nagase, F., Kitamoto, S., & Koyama, K. 1991, PASJ, 43, 501
- Mihara, T., Ph.D. thesis in University of Tokyo 1995
- Mihara, T., Makishima, K., & Nagase, F. 1998, Adv. Space Res. 22, 987
- Mihara, T., Makishima, K., & Nagase, F. 2004, ApJ, 610, 390
- Nagase, F., 1989, PASJ, 41, 1
- Nagase, F., Dotani, T., Tanaka, Y., Makishima, K., Mihara, T., Sakao, T., Tsunemi, H., Kitamoto, S., Tamura, K., Yoshida, A., & Nakamura, H. 1991, ApJ, 375, L49
- Negueruela, I. & Okazaki, A. T. 2001, A&A, 369, 108
- Okada, Y., Niko, H., Makishima, K., Nakajima, M., Mihara, T., Terada, Y., Nagase, F., & Tanaka, Y. 2004, Proc. 5th INTEGRAL Workshp

- Orlandini, M., dal Fiume, D., Frontera, F., Cusumano, G., del Sordo, S., Giarrusso, S., Piraino, S., Segreto, A., Guainazzi, M., & Piro, L. 1998, *A&A*, 332, 121
- Remillard, R., 2005, *Atel*, 371, 1
- Romanova, M. M., Ustyugova, G. V., Koldoba, A. V., & Lovelace, R. V. E., 2004, *ApJ*, 616, 151
- Rose, L. A., Marshall, F. E., Holt, S. S., Boldt, E. A., Rothschild, R. E., Serlemitsos, P. J., Pravdo, S. H., & Kaluzienski, L. J. 1979, *ApJ*, 231, 919
- Rothschild, R. E., Blanco, P. R., Gruber, D. E., Heindl, W. A., MacDonald, D. R., Marsden, D. C., Pelling, M. R., Wayne, L. R., Hink, P. L. 1998, *ApJ*, 496, 538
- Rybicki, G. B., & Lightman, A. P. 1979, *Radiation Processed in Astrophysics*, John Wiley & Sons, Inc
- Santangelo, A., Segreto, A., Giarrusso, S., dal Fiume, D., Orlandini, M., Parmar, A. N., Oosterbroek, T., Bulik, T., Mihara, T., Campana, S., Israel, G. L., & Stella, L. 1999, *ApJ*, 523, L85
- Swank, J., Remillard, R., & Smith, E. *Atel*, 2004, 349, 1
- Trümper, J., Pietsch, W., Reppin, C., Voges, W., Staubert, R., & Kendziorra, E. 1978, *ApJ*, 219, L105
- Unger, S. J., Roche, P., Negueruela, I., Ringwald, F. A., Lloyd, C., & Coe, M. J. 1998, *A&A* 336, 960
- Wheaton, W. A., Doty, J. P., Primini, F. A., Cooke, B. A., Dobson, C. A., Goldman, A., Hecht, M., Howe, S. K., Hoffman, J. A., & Scheepmaker, A. 1979, *Nature*, 282, 240
- White, N., Swank, J., & Holt, S.S. 1983, *ApJ*, 270, 711
- Wilms, J., Nowak, M. A., Dove, J. B., Fender, R. P., & di Matteo, T. 1999, *ApJ*, 522, 460

Table 1. The log of *RXTE* observations of 4U 0115+63 in the 1999 March–April outburst.

Obs.	Date (1999)	Start/End Time <sup>a</sup> (UT)	PCA			HEXTE	
			PCU. No.	Exposure [ks]	Rate <sup>b</sup> [c s <sup>-1</sup> PCU <sup>-1</sup> ]	Exposure [ks]	Rate <sup>c</sup> [c s <sup>-1</sup> ]
1	Mar 3	03:35/03:49	all	0.57	556 ± 1.1	0.18	48.8 ± 0.9
2	Mar 4	13:08/13:41	0,1,2	1.01	466 ± 1.0	0.15	37.2 ± 0.8
3	Mar 5	20:35/20:57	all	1.28	713 ± 1.4	0.44	70.3 ± 0.6
4	Mar 6	20:47/20:56	all	0.54	806 ± 1.6	0.18	82.8 ± 1.0
5	Mar 7	20:40/20:55	all	0.84	866 ± 1.7	0.29	85.3 ± 0.8
6	Mar 9	06:22/06:36	0,2,3,4	0.81	918 ± 1.8	0.20	93.3 ± 0.9
7	Mar 11	08:41/09:40	0,2	1.60	1020 ± 2.0	0.40	97.7 ± 0.6
8	Mar 13	18:58/19:41	0,2,3,4	0.67	1011 ± 2.0	0.21	104 ± 1.0
9	Mar 14	06:44/06:56	0,2,3	0.68	1055 ± 2.1	0.27	105 ± 1.0
10	Mar 15	07:53/08:17	0,2	0.79	994 ± 2.1	0.28	101 ± 1.0
11	Mar 16	09:33/09:46	0,2	0.25	997 ± 2.4	0.09	99.9 ± 1.4
12	Mar 18	07:49/08:05	0,2,3,4	0.37	949 ± 2.0	0.13	98.5 ± 1.2
13	Mar 19a	04:26/06:13	0,2,3	3.45	924 ± 1.8	1.07	92.7 ± 0.4
14	Mar 19b	12:51/13:12	0,2	0.33	876 ± 2.1	0.10	96.0 ± 1.5
15	Mar 20	03:34/03:57	0,2	0.88	857 ± 1.8	0.22	85.2 ± 0.9
16	Mar 21a	06:27/08:33	0,2,3,4	4.13	875 ± 1.7	1.46	91.2 ± 0.3
17	Mar 21b	12:48/13:27	0,2,3,4	0.93	852 ± 1.7	0.29	88.9 ± 0.9
18	Mar 22	04:22/05:28	0,2	3.11	788 ± 1.6	1.06	82.0 ± 0.4
19	Mar 27	07:53/11:01	all	4.02	564 ± 1.2	1.42	60.2 ± 0.4
20	Mar 29	00:12/03:01	0,1,2,3	4.26	517 ± 1.1	1.40	49.2 ± 0.3
21	Mar 31	04:11/06:24	0,2,3	4.11	456 ± 1.0	1.41	41.5 ± 0.3
22	Apr 1	03:27/04:19	0,1,2	0.27	437 ± 1.2	0.09	37.8 ± 1.1
23	Apr 2	04:09/06:14	all	3.63	399 ± 0.8	1.16	32.7 ± 0.4
24	Apr 3	02:30/02:45	0,2,3	0.50	385 ± 0.9	0.16	30.8 ± 1.0
25	Apr 4	04:08/06:11	all	3.47	345 ± 0.7	1.16	26.9 ± 0.4
26	Apr 5	11:09/11:27	0,2,3	0.89	309 ± 0.7	0.33	23.0 ± 0.6
27	Apr 6	02:25/04:28	all	3.80	287 ± 0.6	1.25	20.8 ± 0.3
28	Apr 8	01:13/03:27	0,2,3,4	4.66	254 ± 0.6	1.56	17.3 ± 0.3
29	Apr 10	03:59/06:05	all	3.48	210 ± 0.5	1.18	12.1 ± 0.3
30	Apr 12	02:16/04:28	0,1,2,3	4.12	146 ± 0.3	1.36	8.6 ± 0.3
31	Apr 14	01:14/03:22	all	3.94	111 ± 0.2	1.31	6.8 ± 0.3
32	Apr 16	21:58/22:12	0,1,2,4	0.83	60.1 ± 0.2	0.28	2.9 ± 0.6
33	Apr 18	21:56/22:10	0,2,3,4	0.82	24.9 ± 0.1	0.28	1.9 ± 0.6
34	Apr 20	01:14/01:34	all	0.64	12.4 ± 0.1	0.22	0.7 ± 0.6

<sup>a</sup>Start and end time (UT) of the PCA observations.

<sup>b</sup>In the 3-30 keV energy range.

<sup>c</sup>Count rates of HEXTE cluster A in the 15-50 keV energy range.

Table 2. Summary of the best-fit parameters of the NPEX×CYAB(×CYAB) model, determined by the date-sorted PCA spectra from March 27 thorough April 8.

Date	$A_1$ (ph s <sup>-1</sup> keV <sup>-1</sup> )	$\alpha_1$	$A_2^a$ (ph s <sup>-1</sup> keV <sup>-1</sup> )	$kT$ (keV)	$E_{a1}^b$ (keV)	$W_1$ (keV)	$\tau_1$	$W_2$ (keV)	$\tau_2$	$L_x^c$	$\chi_\nu^2$
Mar 27	0.50 <sup>+0.45</sup> <sub>-0.22</sub>	1.49 <sup>+0.53</sup> <sub>-0.49</sub>	7.92 <sup>+1.15</sup> <sub>-1.83</sub>	4.91 <sup>+1.12</sup> <sub>-0.43</sub>	10.6 <sup>+0.1</sup> <sub>-0.1</sub>	5.91 <sup>+0.17</sup> <sub>-0.15</sub>	0.89 <sup>+0.05</sup> <sub>-0.05</sub>	6.80 <sup>+1.93</sup> <sub>-1.29</sub>	1.12 <sup>+0.51</sup> <sub>-0.25</sub>	6.79	0.62
Mar 29	0.57 <sup>+0.50</sup> <sub>-0.25</sub>	1.67 <sup>+0.53</sup> <sub>-0.49</sub>	7.88 <sup>+0.82</sup> <sub>-1.24</sub>	4.61 <sup>+0.61</sup> <sub>-0.28</sub>	10.6 <sup>+0.1</sup> <sub>-0.1</sub>	6.59 <sup>+0.27</sup> <sub>-0.25</sub>	0.85 <sup>+0.06</sup> <sub>-0.04</sub>	5.91 <sup>+1.67</sup> <sub>-1.18</sub>	0.91 <sup>+0.34</sup> <sub>-0.19</sub>	6.04	0.89
Mar 31	0.53 <sup>+0.34</sup> <sub>-0.20</sub>	1.68 <sup>+0.40</sup> <sub>-0.38</sub>	6.10 <sup>+0.21</sup> <sub>-0.22</sub>	5.22(fixed)	10.7 <sup>+0.2</sup> <sub>-0.2</sub>	7.78 <sup>+0.29</sup> <sub>-0.26</sub>	0.95 <sup>+0.03</sup> <sub>-0.04</sub>	7.47 <sup>+0.69</sup> <sub>-0.67</sub>	1.03 <sup>+0.07</sup> <sub>-0.08</sub>	5.25	0.75
Apr 2	0.61 <sup>+0.25</sup> <sub>-0.22</sub>	1.84 <sup>+0.28</sup> <sub>-0.37</sub>	5.26 <sup>+0.13</sup> <sub>-0.18</sub>	5.39(fixed)	11.5 <sup>+0.3</sup> <sub>-0.3</sub>	10.25 <sup>+0.76</sup> <sub>-0.49</sub>	1.12 <sup>+0.05</sup> <sub>-0.06</sub>	6.33 <sup>+1.65</sup> <sub>-1.93</sub>	0.59 <sup>+0.15</sup> <sub>-0.20</sub>	4.61	1.13
Apr 3	0.61 <sup>+0.55</sup> <sub>-0.27</sub>	1.79 <sup>+0.53</sup> <sub>-0.47</sub>	6.59 <sup>+0.90</sup> <sub>-1.10</sub>	3.88 <sup>+0.70</sup> <sub>-0.33</sub>	13.6 <sup>+0.5</sup> <sub>-1.0</sub>	8.94 <sup>+2.27</sup> <sub>-1.63</sub>	0.88 <sup>+0.22</sup> <sub>-0.17</sub>	—	—	4.24	0.90
Apr 4	0.57 <sup>+0.37</sup> <sub>-0.21</sub>	1.85 <sup>+0.41</sup> <sub>-0.38</sub>	5.80 <sup>+0.45</sup> <sub>-0.49</sub>	3.95 <sup>+0.32</sup> <sub>-0.22</sub>	13.8 <sup>+0.4</sup> <sub>-0.5</sub>	9.05 <sup>+1.16</sup> <sub>-0.98</sub>	0.93 <sup>+0.11</sup> <sub>-0.10</sub>	—	—	3.85	0.93
Apr 5	0.31 <sup>+0.22</sup> <sub>-0.11</sub>	1.46 <sup>+0.42</sup> <sub>-0.38</sub>	3.93 <sup>+0.88</sup> <sub>-1.01</sub>	4.96 <sup>+2.59</sup> <sub>-0.83</sub>	13.2 <sup>+0.8</sup> <sub>-1.6</sub>	11.28 <sup>+2.89</sup> <sub>-2.02</sub>	1.27 <sup>+0.26</sup> <sub>-0.24</sub>	—	—	3.42	0.60
Apr 6	0.43 <sup>+0.28</sup> <sub>-0.16</sub>	1.73 <sup>+0.40</sup> <sub>-0.37</sub>	4.89 <sup>+0.40</sup> <sub>-0.42</sub>	3.92 <sup>+0.32</sup> <sub>-0.22</sub>	13.7 <sup>+0.4</sup> <sub>-0.5</sub>	8.98 <sup>+1.19</sup> <sub>-1.04</sub>	0.91 <sup>+0.11</sup> <sub>-0.10</sub>	—	—	3.19	0.97
Apr 8	0.19 <sup>+0.10</sup> <sub>-0.06</sub>	1.14 <sup>+0.35</sup> <sub>-0.30</sub>	3.92 <sup>+0.52</sup> <sub>-0.48</sub>	3.97 <sup>+0.38</sup> <sub>-0.29</sub>	15.0 <sup>+0.3</sup> <sub>-0.4</sub>	8.68 <sup>+1.18</sup> <sub>-1.14</sub>	1.06 <sup>+0.16</sup> <sub>-0.15</sub>	—	—	2.78	0.94

<sup>a</sup> × 10<sup>-3</sup>

<sup>b</sup>The second resonance energy  $E_{a2}$  was fixed at  $2 \times E_{a1}$ .

<sup>c</sup>10<sup>37</sup> erg s<sup>-1</sup> in 3–30 keV

Table 3. The same as Table 2, but for the intensity-sorted PCA spectra.

Region	$A_1$ (ph s <sup>-1</sup> keV <sup>-1</sup> )	$\alpha_1$	$A_2^a$ (ph s <sup>-1</sup> keV <sup>-1</sup> )	$kT$ (keV)	$E_{a1}^b$ (keV)	$W_1$ (keV)	$\tau_1$	$W_2$ (keV)	$\tau_2$	$L_x^c$	$\chi_\nu^2$
f1	0.42 <sup>+0.30</sup> <sub>-0.17</sub>	1.27 <sup>+0.45</sup> <sub>-0.43</sub>	7.20 <sup>+0.39</sup> <sub>-0.46</sub>	5.76(fixed)	10.4 <sup>+0.1</sup> <sub>-0.2</sub>	5.79 <sup>+0.16</sup> <sub>-0.14</sub>	0.95 <sup>+0.03</sup> <sub>-0.03</sub>	7.90 <sup>+0.52</sup> <sub>-0.49</sub>	1.50 <sup>+0.04</sup> <sub>-0.05</sub>	7.47	0.84
f2	0.58 <sup>+0.45</sup> <sub>-0.24</sub>	1.61 <sup>+0.47</sup> <sub>-0.46</sub>	8.76 <sup>+0.28</sup> <sub>-0.34</sub>	4.59(fixed)	10.6 <sup>+0.1</sup> <sub>-0.1</sub>	5.97 <sup>+0.16</sup> <sub>-0.14</sub>	0.85 <sup>+0.02</sup> <sub>-0.02</sub>	5.94 <sup>+0.40</sup> <sub>-0.39</sub>	0.97 <sup>+0.03</sup> <sub>-0.04</sub>	6.81	0.72
f3	0.62 <sup>+0.49</sup> <sub>-0.27</sub>	1.73 <sup>+0.48</sup> <sub>-0.47</sub>	8.46 <sup>+0.25</sup> <sub>-0.30</sub>	4.54(fixed)	10.6 <sup>+0.1</sup> <sub>-0.1</sub>	6.37 <sup>+0.19</sup> <sub>-0.16</sub>	0.84 <sup>+0.02</sup> <sub>-0.02</sub>	5.92 <sup>+0.41</sup> <sub>-0.42</sub>	0.89 <sup>+0.04</sup> <sub>-0.04</sub>	6.33	0.68
f4	0.83 <sup>+0.86</sup> <sub>-0.43</sub>	2.05 <sup>+0.59</sup> <sub>-0.61</sub>	7.69 <sup>+0.84</sup> <sub>-1.93</sub>	4.44 <sup>+1.07</sup> <sub>-0.28</sub>	10.7 <sup>+0.1</sup> <sub>-0.2</sub>	7.48 <sup>+0.39</sup> <sub>-0.42</sub>	0.84 <sup>+0.09</sup> <sub>-0.05</sub>	5.73 <sup>+3.10</sup> <sub>-1.62</sub>	0.70 <sup>+0.61</sup> <sub>-0.21</sub>	5.39	0.64
f5	0.99 <sup>+0.76</sup> <sub>-0.41</sub>	2.26 <sup>+0.46</sup> <sub>-0.43</sub>	6.48 <sup>+0.38</sup> <sub>-0.40</sub>	4.71 <sup>+0.20</sup> <sub>-0.17</sub>	10.9 <sup>+0.3</sup> <sub>-0.2</sub>	11.38 <sup>+0.52</sup> <sub>-0.67</sub>	0.96 <sup>+0.05</sup> <sub>-0.04</sub>	1.63 <sup>+1.98</sup> <sub>-0.63</sub>	0.21 <sup>+0.07</sup> <sub>-0.04</sub>	4.59	0.91
f6	0.56 <sup>+0.34</sup> <sub>-0.20</sub>	1.84 <sup>+0.39</sup> <sub>-0.36</sub>	5.43 <sup>+0.42</sup> <sub>-0.45</sub>	4.18 <sup>+0.38</sup> <sub>-0.26</sub>	13.3 <sup>+0.5</sup> <sub>-0.6</sub>	10.04 <sup>+1.17</sup> <sub>-1.02</sub>	0.99 <sup>+0.10</sup> <sub>-0.09</sub>	—	—	3.79	0.97
f7	0.29 <sup>+0.16</sup> <sub>-0.10</sub>	1.45 <sup>+0.36</sup> <sub>-0.34</sub>	4.17 <sup>+0.39</sup> <sub>-0.39</sub>	4.21 <sup>+0.41</sup> <sub>-0.29</sub>	13.8 <sup>+0.5</sup> <sub>-0.6</sub>	9.98 <sup>+1.16</sup> <sub>-1.06</sub>	1.06 <sup>+0.11</sup> <sub>-0.11</sub>	—	—	2.99	0.86
f8	0.15 <sup>+0.16</sup> <sub>-0.05</sub>	0.99 <sup>+0.60</sup> <sub>-0.38</sub>	3.48 <sup>+1.28</sup> <sub>-1.03</sub>	4.14 <sup>+1.40</sup> <sub>-0.69</sub>	14.9 <sup>+0.5</sup> <sub>-0.9</sub>	9.24 <sup>+2.75</sup> <sub>-2.60</sub>	1.13 <sup>+0.41</sup> <sub>-0.37</sub>	—	—	2.62	0.73

<sup>a</sup> $\times 10^{-3}$

<sup>b</sup>The second resonance energy was fixed at  $2 \times E_{a1}$ .

<sup>c</sup> $10^{37}$  erg s<sup>-1</sup> in 3–30 keV

Table 4. The best-fit parameters of the date-sorted spectra, incorporating the HEXTE data.

Observation (1999)	$A_1$ ( $\text{ph s}^{-1} \text{keV}^{-1}$ )	$\alpha_1$	$A_2^a$ ( $\text{ph s}^{-1} \text{keV}^{-1}$ )	$kT$ (keV)	$E_{a1}^b$ (keV)	$W_1$ (keV)	$\tau_1$	$W_2$ (keV)	$\tau_2$	$L_x^c$	$\chi_\nu^2$
Mar 3	$0.40^{+0.21}_{-0.13}$	$1.24^{+0.36}_{-0.35}$	$7.47^{+0.56}_{-0.68}$	$4.85^{+0.28}_{-0.16}$	$11.9 \pm 0.3$	$8.60^{+0.37}_{-0.32}$	$1.02 \pm 0.03$	$7.70^{+3.03}_{-2.22}$	$0.59^{+0.19}_{-0.14}$	7.10	0.97
Mar 4	$0.36^{+0.17}_{-0.10}$	$1.20^{+0.32}_{-0.27}$	$4.80^{+0.80}_{-1.76}$	$5.60^{+6.90}_{-0.58}$	$12.8 \pm 0.4$	$9.13^{+0.63}_{-0.48}$	$1.19^{+0.19}_{-0.04}$	$13.97^{+5.91}_{-4.34}$	$1.01^{+1.27}_{-0.33}$	5.55	1.33
Mar 5	$0.56^{+0.35}_{-0.20}$	$1.37^{+0.41}_{-0.37}$	$10.87^{+0.46}_{-0.50}$	$4.66^{+0.09}_{-0.07}$	$10.8^{+0.1}_{-0.2}$	$6.79 \pm 0.15$	$0.91 \pm 0.02$	$7.12^{+0.81}_{-0.63}$	$0.84^{+0.07}_{-0.05}$	9.33	1.37
Mar 6	$0.59^{+0.39}_{-0.21}$	$1.29^{+0.44}_{-0.39}$	$12.07^{+0.61}_{-0.70}$	$4.74^{+0.13}_{-0.09}$	$10.7^{+0.1}_{-0.2}$	$6.31^{+0.13}_{-0.14}$	$0.90 \pm 0.02$	$7.90^{+0.95}_{-0.70}$	$0.95^{+0.08}_{-0.06}$	10.6	1.24
Mar 7	$0.42^{+0.25}_{-0.14}$	$0.89^{+0.40}_{-0.35}$	$11.84^{+0.79}_{-0.88}$	$4.81^{+0.14}_{-0.10}$	$10.8^{+0.2}_{-0.3}$	$7.59^{+0.22}_{-0.21}$	$0.86^{+0.02}_{-0.03}$	$8.41^{+1.41}_{-1.06}$	$0.74^{+0.09}_{-0.07}$	11.3	1.28
Mar 9	$0.51^{+0.28}_{-0.17}$	$0.96^{+0.39}_{-0.36}$	$13.05^{+0.79}_{-0.92}$	$4.67 \pm 0.08$	$10.8 \pm 0.2$	$6.62^{+0.17}_{-0.16}$	$0.85^{+0.02}_{-0.03}$	$7.13^{+0.83}_{-0.75}$	$0.81^{+0.06}_{-0.06}$	12.3	0.85
Mar 11	$0.70^{+0.41}_{-0.23}$	$1.14^{+0.40}_{-0.34}$	$14.75^{+0.78}_{-0.84}$	$4.69^{+0.08}_{-0.06}$	$10.6^{+0.1}_{-0.2}$	$5.97^{+0.11}_{-0.10}$	$0.88 \pm 0.02$	$8.34^{+0.68}_{-0.52}$	$0.96^{+0.05}_{-0.04}$	13.1	1.18
Mar 13	$0.69^{+0.46}_{-0.24}$	$1.17^{+0.44}_{-0.38}$	$15.00^{+0.82}_{-0.93}$	$4.66^{+0.10}_{-0.08}$	$10.5 \pm 0.1$	$5.34 \pm 0.09$	$0.86^{+0.02}_{-0.03}$	$7.99^{+0.74}_{-0.55}$	$1.02^{+0.06}_{-0.05}$	13.6	1.37
Mar 14	$0.41^{+0.22}_{-0.13}$	$0.70^{+0.39}_{-0.35}$	$14.27^{+1.02}_{-1.19}$	$4.65^{+0.10}_{-0.07}$	$10.8^{+0.1}_{-0.2}$	$5.78^{+0.12}_{-0.11}$	$0.80 \pm 0.03$	$8.13^{+0.87}_{-0.68}$	$0.89^{+0.06}_{-0.05}$	14.1	1.23
Mar 15	$0.88^{+0.67}_{-0.32}$	$1.40^{+0.48}_{-0.40}$	$14.88^{+0.76}_{-0.83}$	$4.71^{+0.12}_{-0.08}$	$10.4^{+0.1}_{-0.2}$	$5.34^{+0.11}_{-0.10}$	$0.86 \pm 0.02$	$9.04^{+0.89}_{-0.58}$	$1.08^{+0.07}_{-0.05}$	12.9	1.56
Mar 16	$0.80^{+0.70}_{-0.34}$	$1.31^{+0.54}_{-0.48}$	$14.66^{+1.01}_{-1.19}$	$4.67^{+0.18}_{-0.13}$	$10.6 \pm 0.2$	$5.56^{+0.17}_{-0.15}$	$0.86 \pm 0.03$	$8.74^{+1.32}_{-1.00}$	$0.97^{+0.10}_{-0.08}$	13.1	1.21
Mar 18	$0.55^{+0.37}_{-0.20}$	$1.03^{+0.44}_{-0.39}$	$13.95^{+0.90}_{-1.04}$	$4.55^{+0.14}_{-0.10}$	$10.7^{+0.1}_{-0.2}$	$5.37 \pm 0.11$	$0.81 \pm 0.03$	$7.76^{+1.07}_{-0.78}$	$0.94^{+0.09}_{-0.06}$	12.7	1.47
Mar 19a	$0.56^{+0.34}_{-0.17}$	$1.10^{+0.41}_{-0.31}$	$13.29^{+0.68}_{-0.65}$	$4.69^{+0.06}_{-0.04}$	$10.5^{+0.1}_{-0.1}$	$5.35^{+0.08}_{-0.07}$	$0.83^{+0.02}_{-0.02}$	$8.74^{+0.52}_{-0.34}$	$1.00^{+0.04}_{-0.03}$	12.4	2.16
Mar 19b	$0.70^{+0.51}_{-0.28}$	$1.30^{+0.47}_{-0.43}$	$13.07^{+0.80}_{-1.00}$	$4.54^{+0.13}_{-0.11}$	$10.7^{+0.1}_{-0.2}$	$5.16^{+0.13}_{-0.13}$	$0.87^{+0.03}_{-0.03}$	$7.55^{+1.17}_{-0.81}$	$1.00^{+0.11}_{-0.07}$	11.5	1.14
Mar 20	$0.85^{+0.58}_{-0.31}$	$1.48^{+0.44}_{-0.39}$	$13.07^{+0.61}_{-0.70}$	$4.58^{+0.11}_{-0.08}$	$10.6 \pm 0.1$	$5.26^{+0.10}_{-0.09}$	$0.88 \pm 0.02$	$7.78^{+0.80}_{-0.59}$	$1.01^{+0.07}_{-0.05}$	11.2	1.26
Mar 21a	$0.57^{+0.39}_{-0.19}$	$1.19^{+0.45}_{-0.36}$	$12.82^{+0.63}_{-0.63}$	$4.68^{+0.05}_{-0.04}$	$10.5^{+0.1}_{-0.1}$	$5.61^{+0.08}_{-0.08}$	$0.82^{+0.02}_{-0.02}$	$8.51^{+0.50}_{-0.37}$	$0.95^{+0.04}_{-0.03}$	11.9	2.44
Mar 21b	$0.52^{+0.34}_{-0.19}$	$1.13^{+0.43}_{-0.40}$	$12.44^{+0.67}_{-0.79}$	$4.64^{+0.10}_{-0.08}$	$10.6^{+0.1}_{-0.2}$	$5.66 \pm 0.11$	$0.82 \pm 0.02$	$7.86^{+0.80}_{-0.66}$	$0.93^{+0.06}_{-0.05}$	11.6	1.24
Mar 22	$0.85^{+0.58}_{-0.30}$	$1.61^{+0.44}_{-0.37}$	$12.16^{+0.44}_{-0.46}$	$4.61^{+0.05}_{-0.04}$	$10.5^{+0.1}_{-0.1}$	$5.39^{+0.08}_{-0.08}$	$0.87^{+0.02}_{-0.02}$	$7.93^{+0.48}_{-0.36}$	$0.99^{+0.04}_{-0.03}$	10.4	2.42
Mar 27	$0.85^{+0.81}_{-0.38}$	$1.90^{+0.55}_{-0.47}$	$8.85^{+0.31}_{-0.34}$	$4.72^{+0.06}_{-0.05}$	$10.4^{+0.1}_{-0.1}$	$5.75^{+0.10}_{-0.11}$	$0.85^{+0.02}_{-0.02}$	$7.78^{+0.51}_{-0.37}$	$1.08^{+0.04}_{-0.03}$	7.64	2.09
Mar 29	$0.88^{+0.64}_{-0.41}$	$2.02^{+0.45}_{-0.51}$	$8.12^{+0.24}_{-0.32}$	$4.75^{+0.07}_{-0.06}$	$10.3^{+0.1}_{-0.2}$	$6.24^{+0.15}_{-0.13}$	$0.82^{+0.02}_{-0.02}$	$8.34^{+0.55}_{-0.46}$	$1.07^{+0.05}_{-0.05}$	6.80	2.73
Mar 31	$0.71^{+0.56}_{-0.28}$	$1.92^{+0.48}_{-0.42}$	$7.04^{+0.25}_{-0.27}$	$4.75^{+0.10}_{-0.07}$	$10.7^{+0.2}_{-0.3}$	$7.67^{+0.24}_{-0.25}$	$0.86 \pm 0.03$	$7.93^{+0.97}_{-0.73}$	$0.87^{+0.08}_{-0.07}$	5.90	1.53
Apr 1	$1.08^{+1.36}_{-0.56}$	$2.23^{+0.66}_{-0.60}$	$7.10^{+0.53}_{-0.58}$	$4.58^{+0.23}_{-0.17}$	$11.5^{+0.3}_{-0.4}$	$8.70^{+0.72}_{-0.57}$	$1.05 \pm 0.06$	$5.13^{+3.19}_{-2.41}$	$0.56^{+0.23}_{-0.18}$	5.28	0.76
Apr 2	$1.01^{+0.71}_{-0.40}$	$2.24^{+0.42}_{-0.40}$	$6.24^{+0.25}_{-0.26}$	$4.77^{+0.18}_{-0.10}$	$11.4^{+0.2}_{-0.3}$	$10.84^{+0.90}_{-0.72}$	$1.04^{+0.03}_{-0.04}$	$3.58^{+2.54}_{-2.27}$	$0.26^{+0.14}_{-0.08}$	4.89	1.16
Apr 3	$0.50^{+0.37}_{-0.20}$	$1.68^{+0.46}_{-0.43}$	$4.94^{+0.39}_{-0.37}$	$5.36^{+0.56}_{-0.45}$	$12.1^{+0.8}_{-0.9}$	$12.48^{+1.08}_{-1.05}$	$1.22 \pm 0.06$	= $W_1$	$\leq 0.69$	4.78	0.96
Apr 4	$0.70^{+0.44}_{-0.26}$	$2.03^{+0.40}_{-0.37}$	$4.84 \pm 0.19$	$5.00^{+0.22}_{-0.20}$	$12.3^{+0.4}_{-0.5}$	$11.89^{+0.94}_{-0.53}$	$1.20 \pm 0.03$	= $W_1$	$\leq 0.54$	4.19	1.14
Apr 5	$0.37^{+0.24}_{-0.14}$	$1.60^{+0.41}_{-0.38}$	$4.02^{+0.28}_{-0.26}$	$5.14^{+0.41}_{-0.34}$	$12.7^{+0.6}_{-0.7}$	$12.05^{+0.94}_{-0.87}$	$1.27 \pm 0.06$	= $W_1$	$\leq 0.63$	3.77	0.67
Apr 6	$0.49^{+0.31}_{-0.18}$	$1.88^{+0.40}_{-0.37}$	$3.93 \pm 0.18$	$5.19^{+0.29}_{-0.25}$	$11.9^{+0.5}_{-0.6}$	$12.36^{+0.62}_{-0.59}$	$1.21 \pm 0.03$	= $W_1$	$\leq 0.61$	3.47	1.21
Apr 8	$0.19^{+0.09}_{-0.06}$	$1.14^{+0.32}_{-0.30}$	$3.30^{+0.20}_{-0.19}$	$4.69^{+0.22}_{-0.20}$	$14.2 \pm 0.4$	$10.89^{+0.64}_{-0.60}$	$1.32^{+0.05}_{-0.06}$	= $W_1$	$\leq 0.49$	3.00	1.17
Apr 10	$0.13^{+0.05}_{-0.04}$	$0.82^{+0.28}_{-0.26}$	$2.79^{+0.25}_{-0.24}$	$4.25^{+0.26}_{-0.22}$	$14.9 \pm 0.4$	$9.67^{+0.87}_{-0.82}$	$1.17^{+0.09}_{-0.10}$	-	-	2.39	0.87
Apr 12	$0.11^{+0.04}_{-0.03}$	$0.87^{+0.24}_{-0.23}$	$1.91^{+0.29}_{-0.25}$	$4.17^{+0.48}_{-0.37}$	$14.7^{+0.5}_{-0.7}$	$10.01^{+1.52}_{-1.43}$	$1.07^{+0.16}_{-0.17}$	-	-	1.63	0.94
Apr 14	$0.13^{+0.05}_{-0.03}$	$1.22^{+0.25}_{-0.21}$	$1.32^{+0.21}_{-0.16}$	$4.61^{+0.56}_{-0.67}$	$14.9^{+0.4}_{-0.6}$	$10.76^{+1.34}_{-1.29}$	$1.32^{+0.15}_{-0.18}$	-	-	1.27	1.00
Apr 16	$0.12^{+0.10}_{-0.04}$	$1.45^{+0.42}_{-0.28}$	$0.84^{+0.34}_{-0.20}$	$3.92^{+0.73}_{-0.61}$	$15.4^{+0.4}_{-0.2}$	$7.41^{+2.32}_{-2.53}$	$1.03^{+0.35}_{-0.39}$	-	-	0.69	1.19
Apr 18	$0.04^{+0.03}_{-0.01}$	$1.18^{+0.36}_{-0.24}$	$0.24^{+0.12}_{-0.10}$	$4.32^{+1.75}_{-0.73}$	$16.4^{+0.6}_{-0.6}$	$5.03^{+3.16}_{-2.25}$	$1.06^{+0.65}_{-0.39}$	-	-	0.34	1.36
Apr 20	$0.02^{+0.03}_{-0.01}$	$1.25^{+0.56}_{-0.36}$	$0.12^{+0.09}_{-0.07}$	$4.08^{+1.96}_{-0.77}$	$15.9^{+1.2}_{-1.3}$	$3.84^{+5.35}_{-2.74}$	$0.80^{+1.06}_{-0.39}$	-	-	0.17	0.90

<sup>a</sup> $\times 10^{-3}$

<sup>b</sup>The value of  $E_{a2}$  was fixed at twice  $E_{a1}$ .

<sup>c</sup> $10^{37} \text{ erg s}^{-1}$  in 3–50 keV

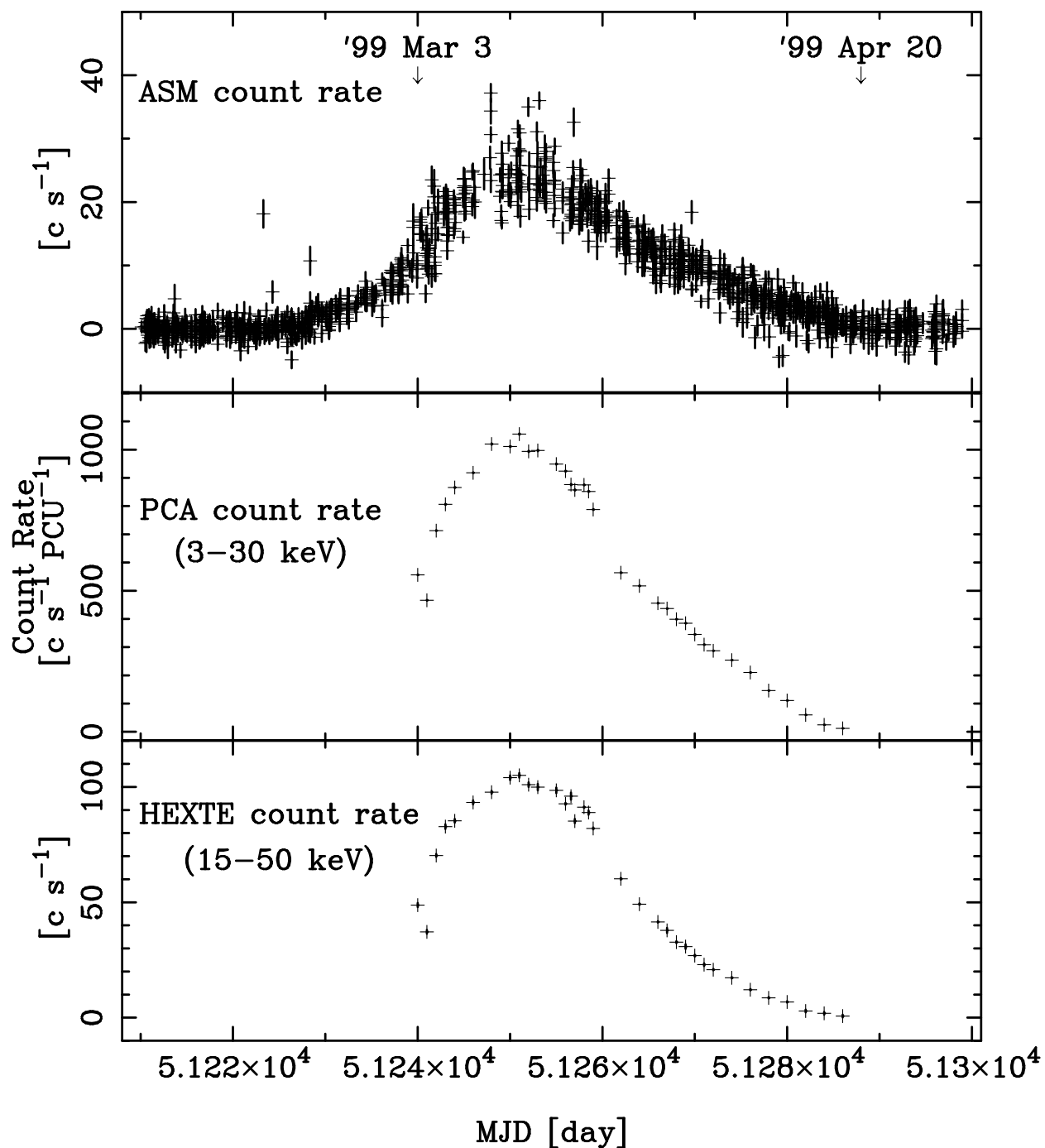


Fig. 1.— (top) The 2–10 keV *RXTE* ASM light curve of 4U 0115+63 in the 1999 March–April outburst. (middle and bottom) The 3–30 keV PCA and the 15–50 keV HEXTE light curves obtained from the 33 pointing observations listed on Table 1.

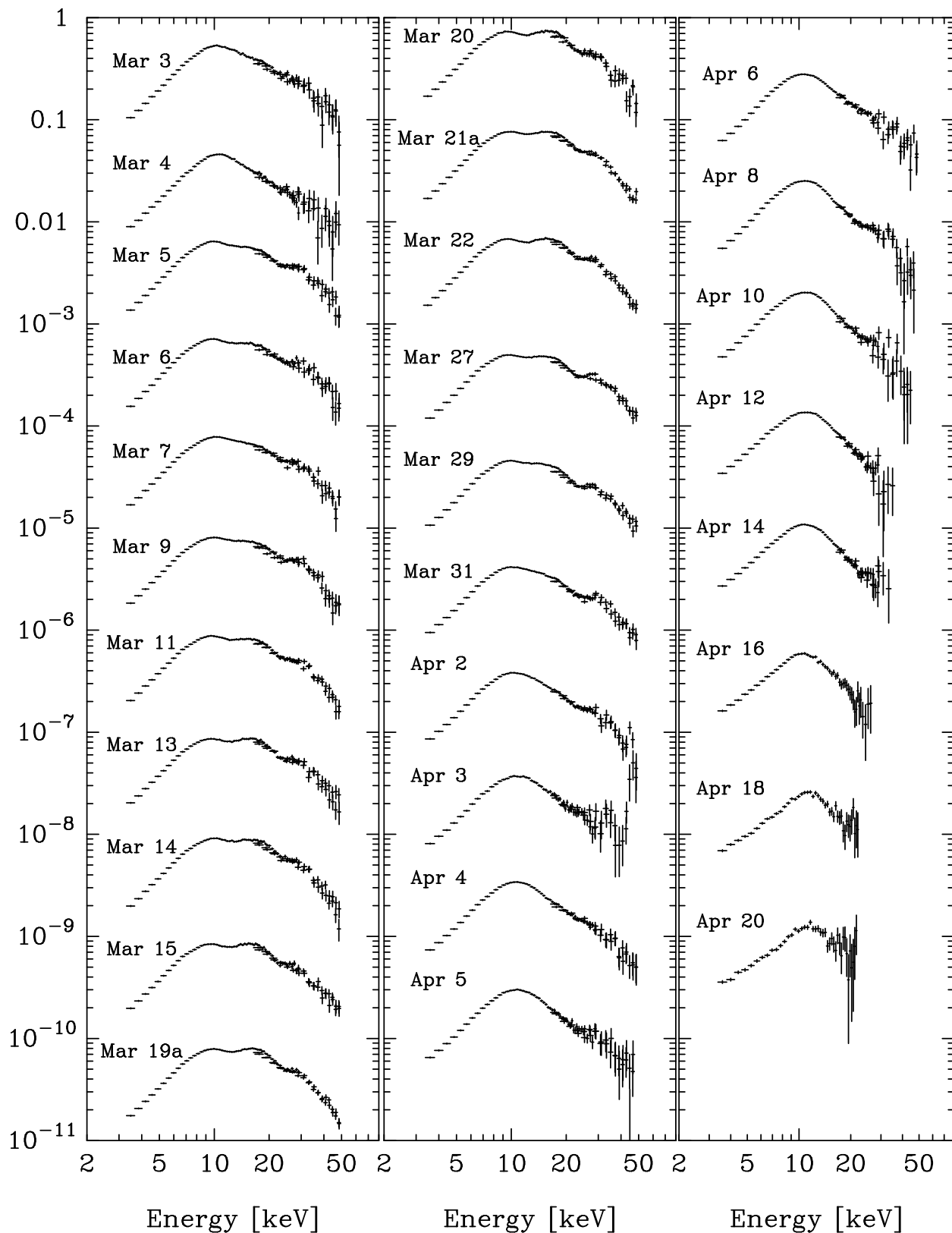


Fig. 2.— Background-subtracted PCA and HEXTE spectra of 4U 0115+63 in the 1999 outburst, shown normalized to those of the Crab Nebula measured by respective instruments. Above plot exclude the same observation date(March 19b, 21b), low exposure data (March 16, 18 and April 1).

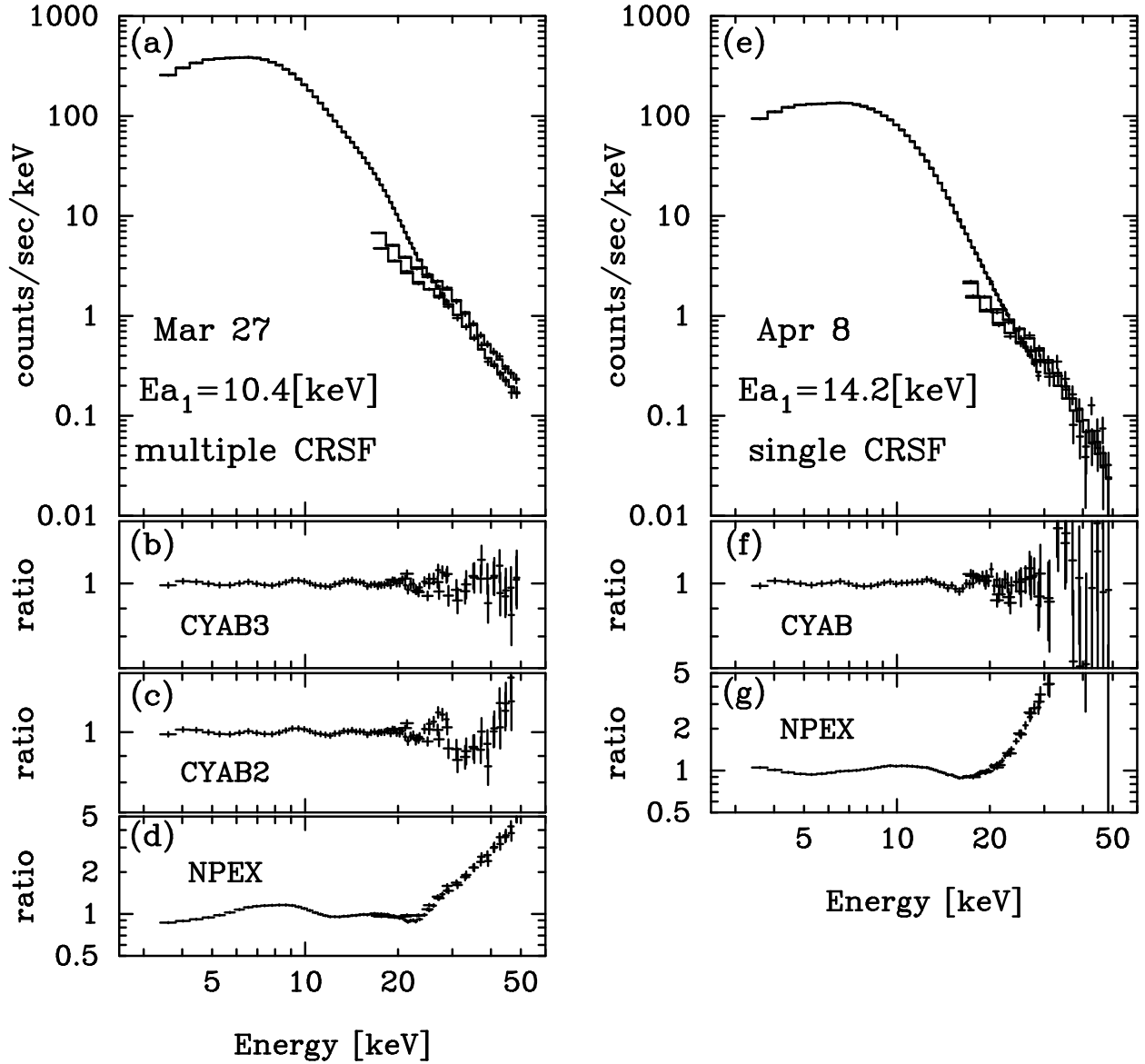


Fig. 3.— Pulse-phase-averaged spectra of 4U 0115+63 on March 27 (left) and April 8 (right). The top panels ((a) and (e)) are the background-subtracted spectra of the PCA and HEXTE, shown in comparison with the best-fit  $\text{NPEX} \times \text{CYAB}$  model (histograms). Two resonances are incorporated to fit the March 27 data, while a single resonance for the April 8 data. The ratios from the NPEX model fits are shown in the bottom panels ((d) and (g)), whereas those from the NPEX model with triple (b), double (c) and single (f) CRSF are shown in the middle panels.

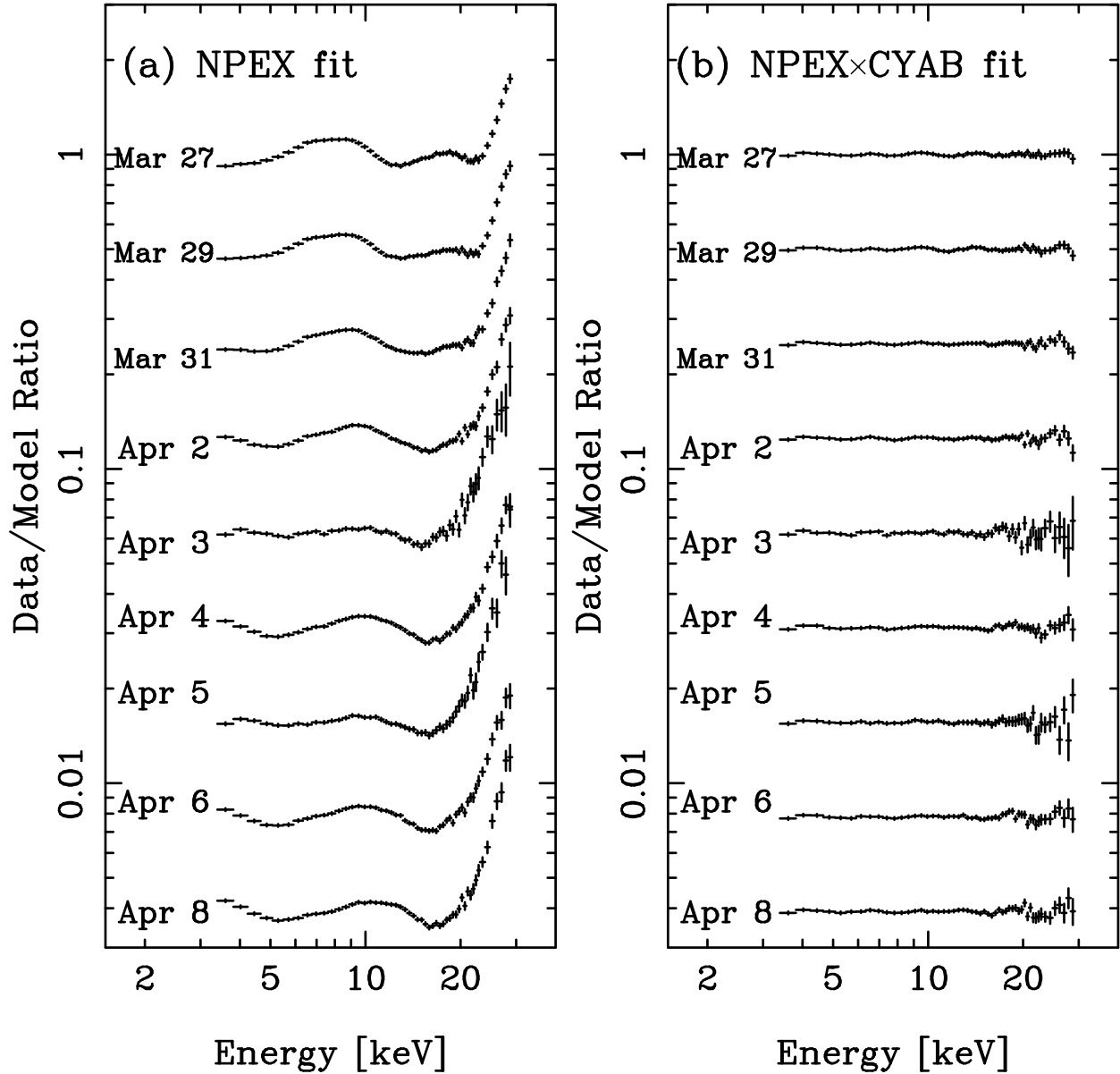


Fig. 4.— (a) Date-sorted PCA spectra of 4U 0115+63 from March 27 to April 8, normalized to the respective best-fit NPEX models. For the presentation, the results are shifted vertically by a factor of 0.5 for each observation. (b) The same as panel (a), but the fitting model is NPEX×CYAB2 (March 27 through April 2) or NPEX×CYAB (April 4 and later).

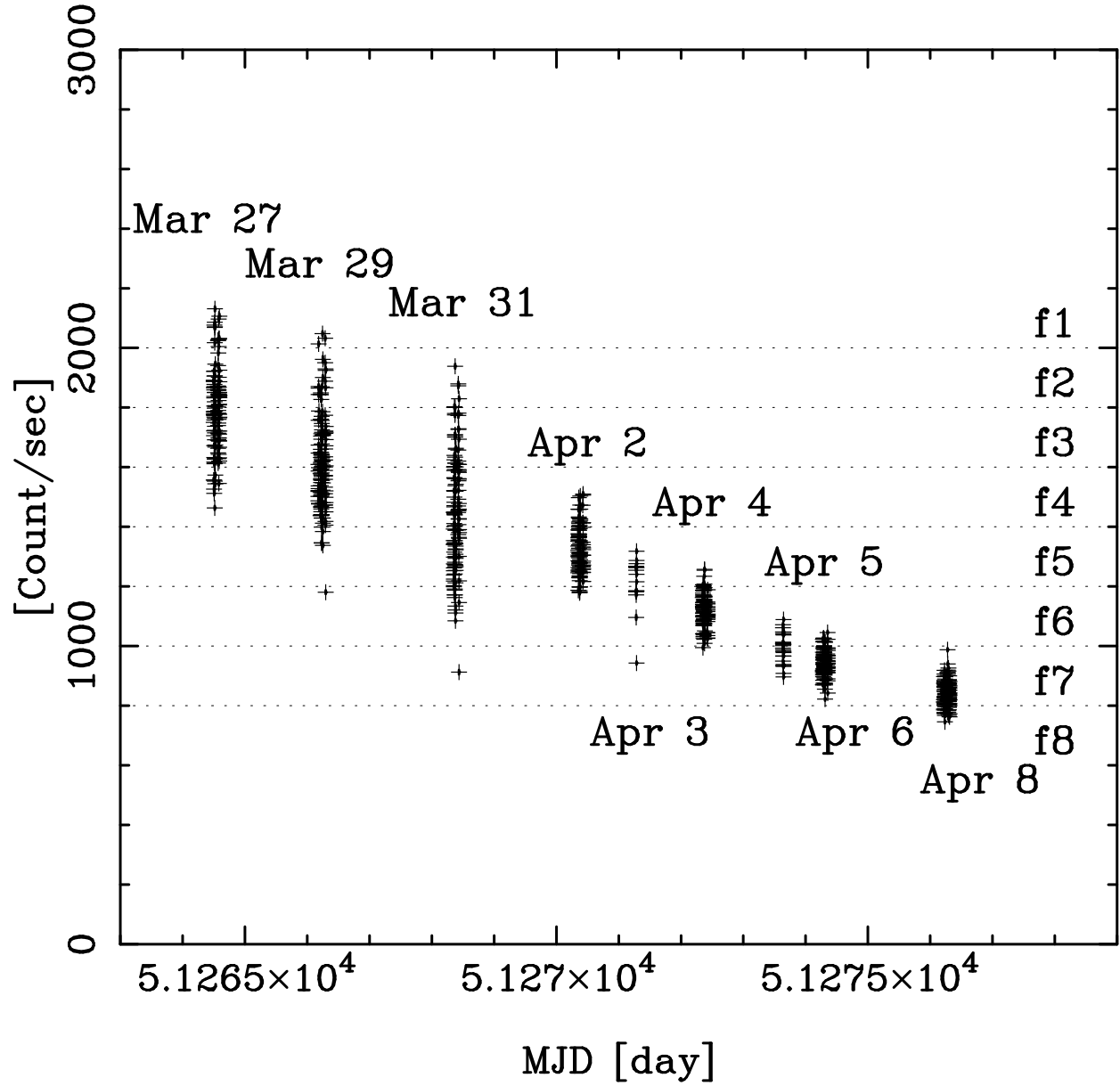


Fig. 5.— The PCU 0 + 2 + 3 light curve of 4U 0115+63 observed from March 27 to April 8, plotted with 16 sec binnings. The horizontal dashed lines indicate boundaries of the intensity sorting.

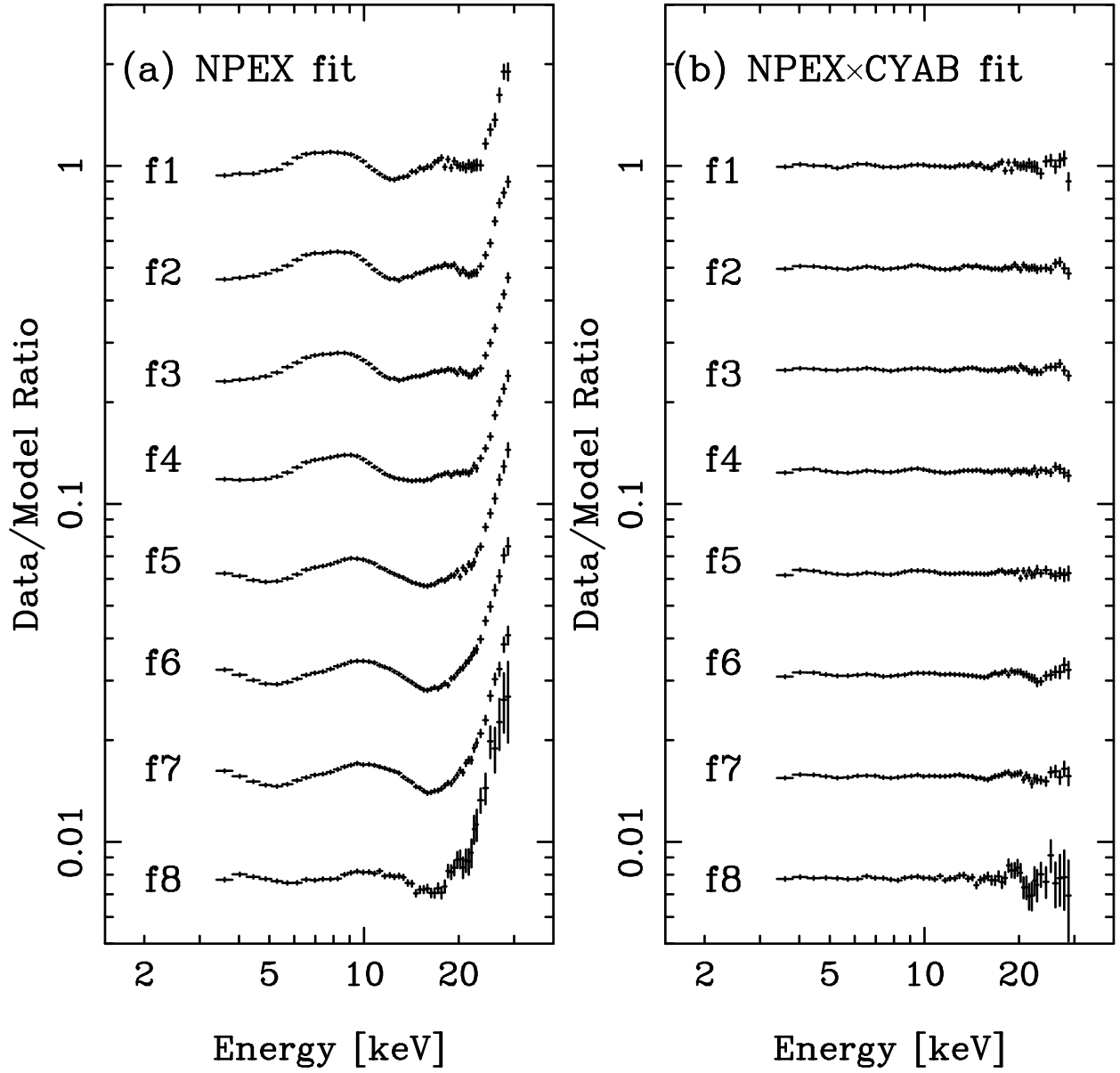


Fig. 6.— (a) The same as Figure 4a, but for the intensity-sorted spectra defined in Figure 5. (b) The intensity-sorted PCA spectra, each normalized to the best-fit NPEX×CYAB2 (f1-f5) or NPEX×CYAB (f6-f8) model. Data are presented in the same manner as Figure 4.

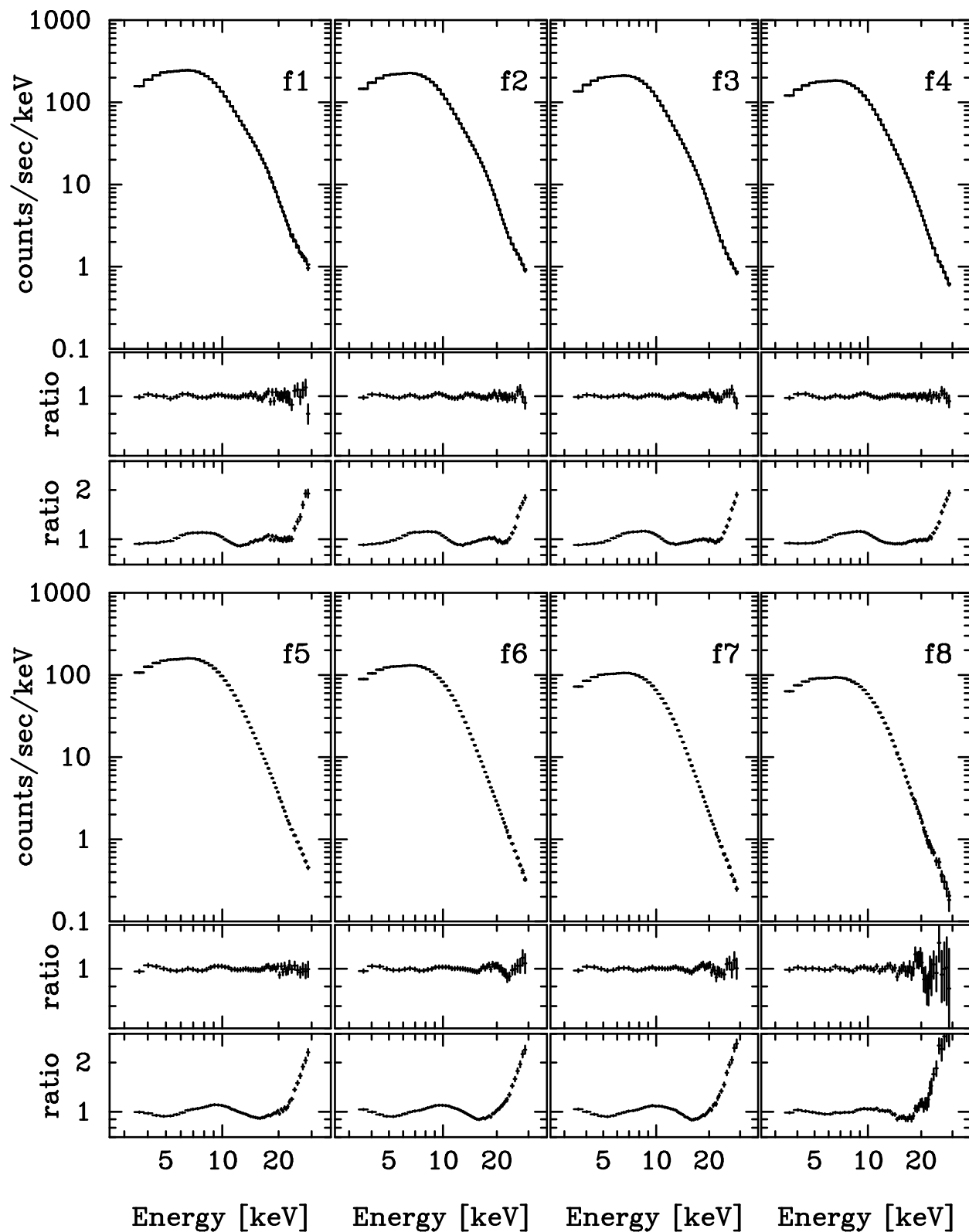


Fig. 7.— The eight intensity-sorted spectra defined in Figure 5, fitted with the NPEX×CYAB2 (f1-f5) or the NPEX×CYAB (f6-f8) model. The middle panels show the data to model ratios, while the bottom panels are the same ratios but without incorporating the CYAB factor(s).

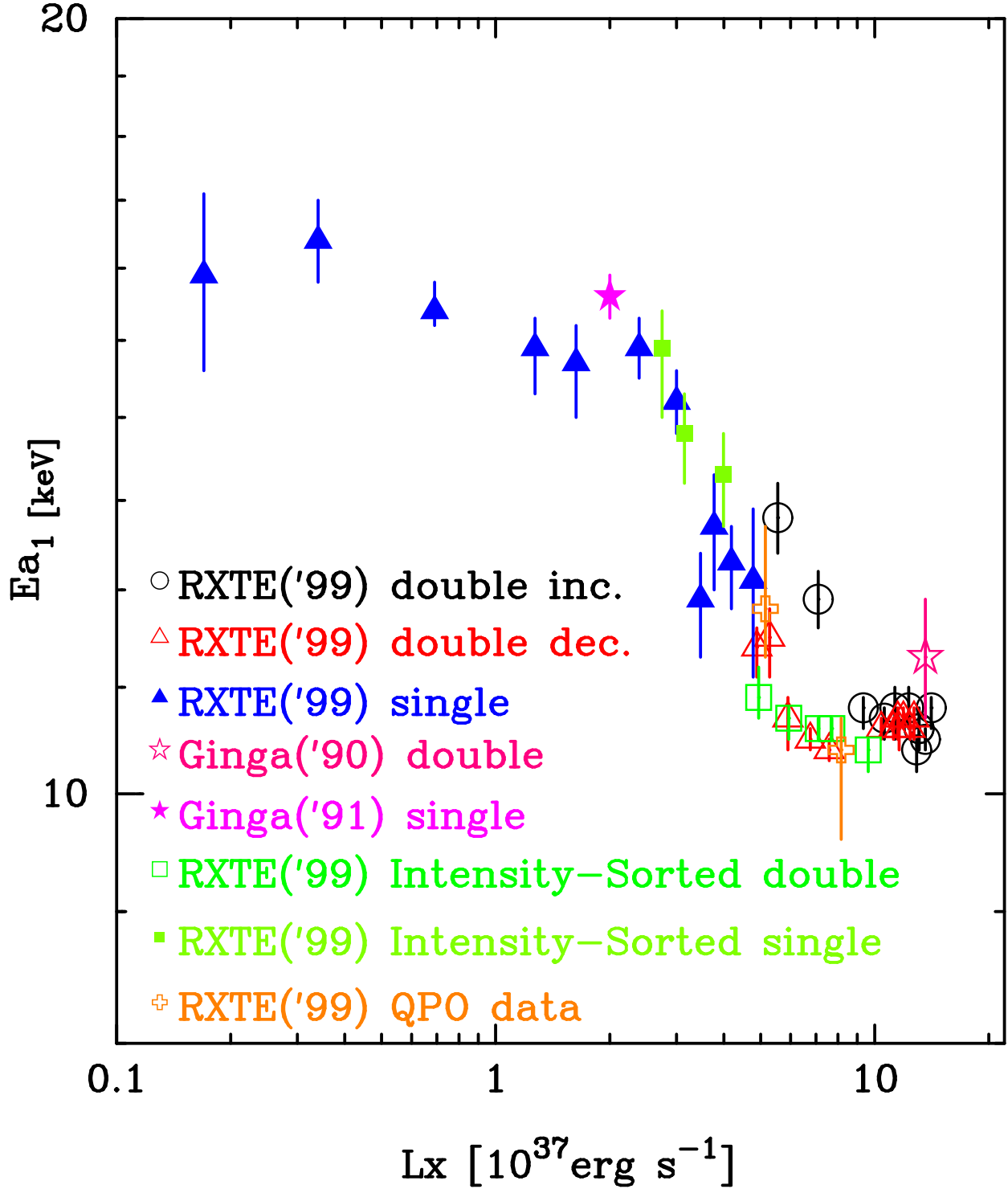


Fig. 8.— The obtained fundamental cyclotron energies shown against the 3 – 50 keV luminosity. The open symbols represent the fundamental energy of the double absorption features, and the filled symbols the energy of the single CRSF. All the date-sorted data in the brightening (circles) and declining (triangles) are presented together with the intensity-sorted (squares) results. The *Ginga* results (Paper 1) are also included with asterisks.

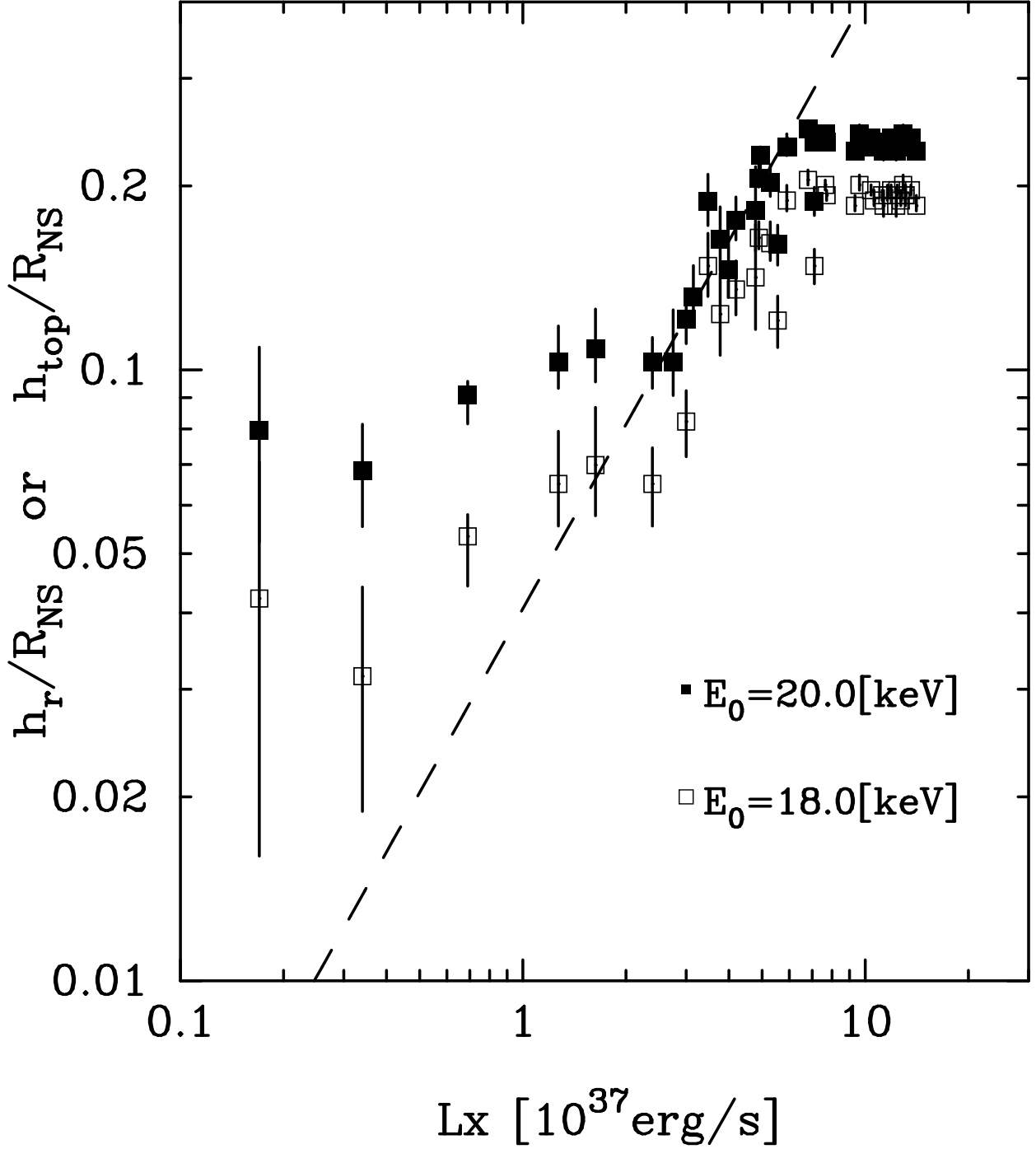


Fig. 9.— The same as Figure 8, but the resonance energy is converted through equation 4 into the height ( $h_r$ ) at which the resonance occurs. The dashed line represents the value of the column top height,  $h_{\text{top}}$ , calculated by equation 5.

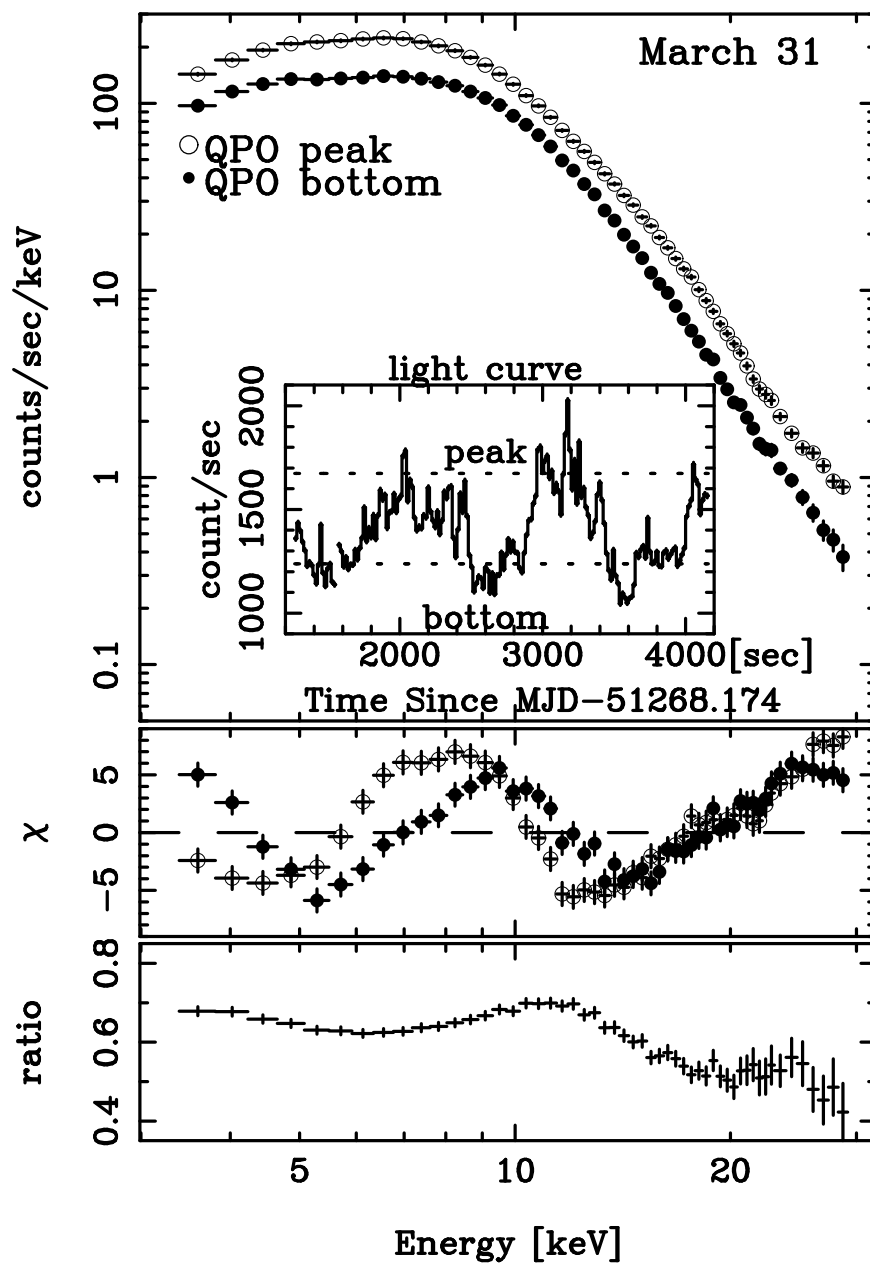


Fig. 10.— Spectral changes associated with a 1 mHz QPO observed on March 31. The top panel shows the background-subtracted PCA spectra accumulated at peaks and bottoms of the QPO, as specified on the 2–30 keV light curve (inset). The middle panel is the residuals from NPEX fits to the two spectra. The bottom panel show the QPO bottom-to-peak ratio.

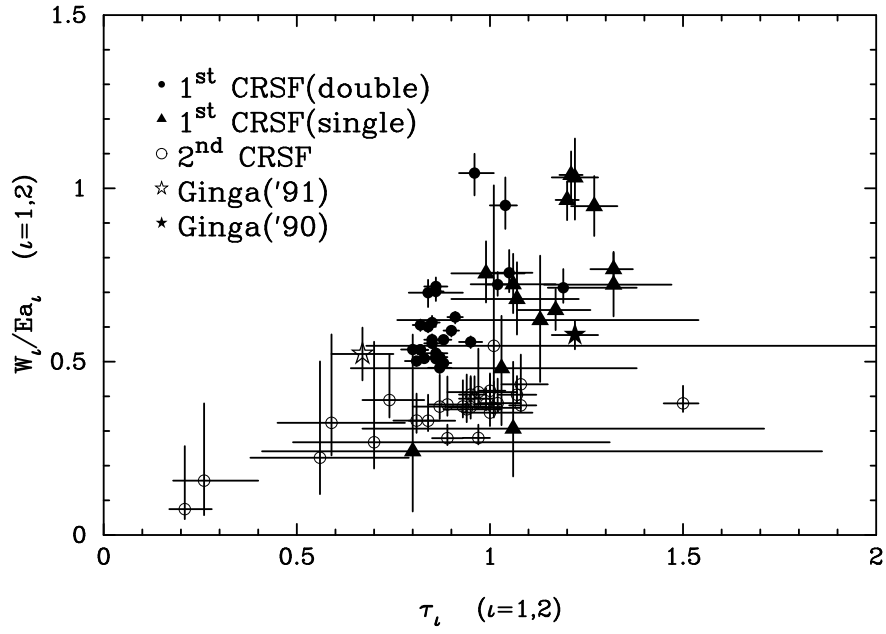


Fig. 11.— The CRSF depth  $\tau$  against the fractional width  $W/E_a$ . The plotted points are obtained from the date-sorted and intensity-sorted analyses.

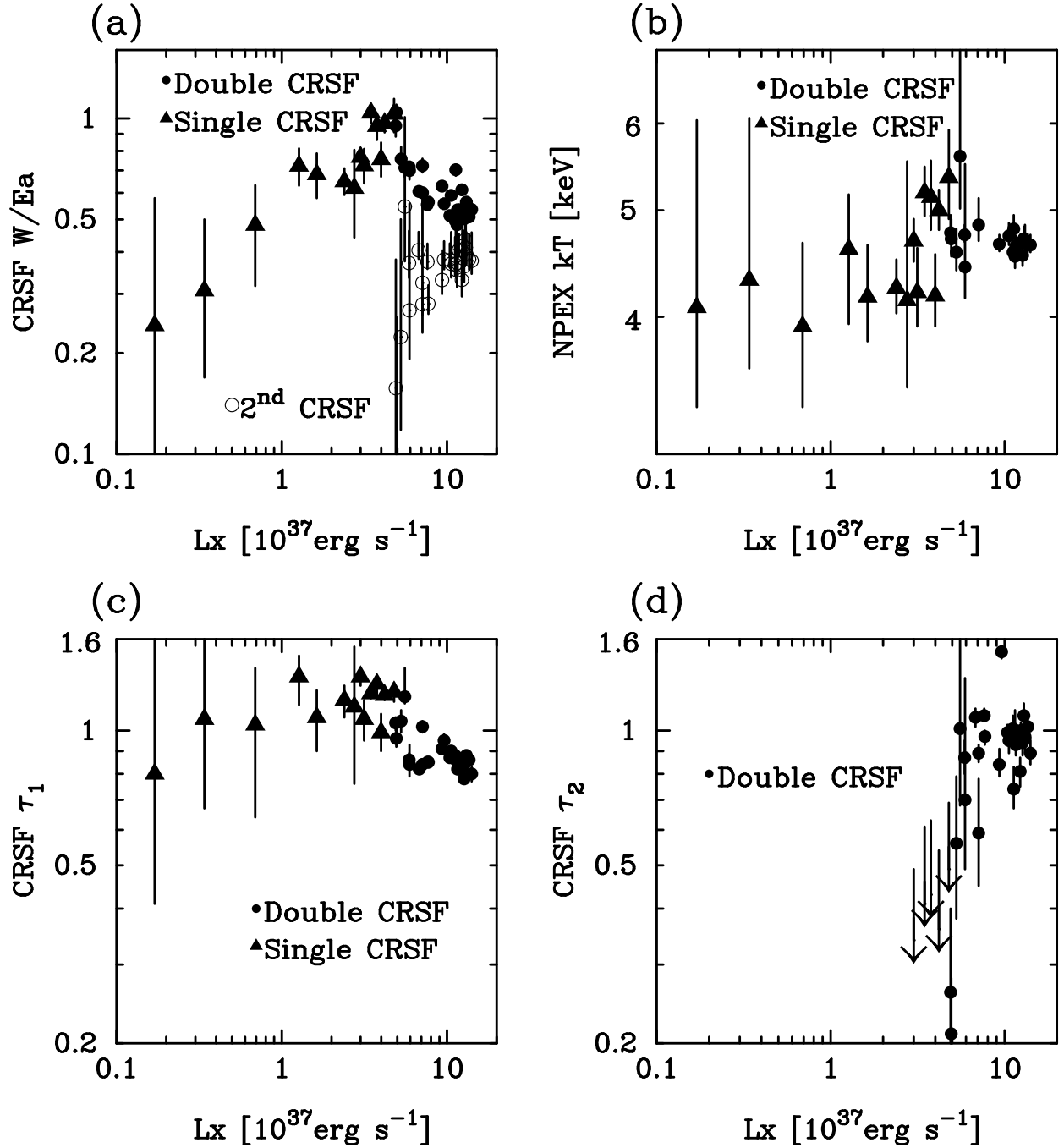


Fig. 12.— The dependence of the CRSF and NPEX parameters on the 3–50 keV luminosity, obtained from the 34 date-sorted data and the 8 intensity-sorted data. The circles and triangles represent those spectra which are described by the double and single CRSF factor(s), respectively. (a) The  $W/Ea$  ratio for the fundamental and second harmonic resonances. (b) The NPEX  $kT$ . (c) The fundamental resonance depth,  $\tau_1$ . (d) The second harmonic depth,  $\tau_2$ .